Tetrahedron Green Chem 5 (2025) 100059

Contents lists available at ScienceDirect

Tetrahedron Green Chem

journal homepage: www.journals.elsevier.com/tetrahedron-green-chem

Comparing the photocatalytic activity of suspended and floating Ag-decorated TiO_2 for dye removal

Nila Davari [a], Ermelinda Falletta [b,c], Claudia L. Bianchi [b,c], Viviane Yargeau [d], Cristina Rodriguez-Seco [a], Daria C. Boffito [a,e,*]

[a] Department of Chemical Engineering, Polytechnique Montréal, Montréal, Canada
[b] Department of Chemistry, University of Milan, Milan, Italy
[c] Consorzio Interuniversitario Nazionale per la Scienza e Tecnologia dei Materiali (INSTM), via Giusti 9, 50121, Florence, Italy
[d] Department of Chemical Engineering, McGill University, Montréal, Canada
[e] Canada Research Chair in Engineering Process Intensification and Catalysis, Canada

ARTICLE INFO

Keywords:
Ag-decorated
Floating photocatalyst
Spray drying
Suspended photocatalyst
Ultrasonication

ABSTRACT

We proposed a two-step synthesis process to fabricate floating TiO_2 and Ag-decorated TiO_2 (Ag/TiO_2) photocatalysts. In the first step, an ultrasound-assisted sol-gel method followed by spray drying was adopted to synthesize powder photocatalysts. Next, the powder samples were immobilized onto a floating polyurethane foam (PUF) support with an ultrasound-assisted impregnation method. The photocatalytic activity of TiO_2 and Ag/TiO_2 was evaluated to remove methyl orange (MO) as a dye pollutant in two suspended and floating photocatalytic systems. Ag decoration on TiO_2 improved the optical and textural properties by narrowing the bandgap energy to 2.9 eV and increasing the surface area from 10 m^2/g to 30 m^2/g. Ag/TiO_2 exhibited higher photocatalytic activity compared to TiO_2 for MO removal, which was 98 % for suspended and 95 % for floating catalysts under simulated sunlight irradiation. In addition, floating photocatalysts exhibited higher photocatalytic activity over five cycles of reuse. Floating Ag/TiO_2@PUF maintained 89 % of its initial photoactivity, while suspended Ag/TiO_2 lost 50 % after the five cycles. Moreover, we investigated the effect of operating conditions on the photocatalytic performance of floating Ag/TiO_2@PUF. Optimal conditions for the complete removal of MO below detection limits were obtained as follows: Ag/TiO_2@PUF loading = 0.4:200 g/mL, initial MO concentration = 5 mg/L, time = 90 min, and pH = 4 under simulated sunlight irradiation. This study highlights the potential of floating photocatalyst systems as a sustainable, reusable, and scalable approach for wastewater treatment, addressing challenges in catalyst recovery and efficiency under real-world conditions.

1. Introduction

TiO_2 as an n-type semiconductor photocatalyst has been investigated for wastewater treatment owing to its super-hydrophilicity, chemical and thermal stability, optical properties, and photocatalytic activity [1–4]. However, the wide bandgap of TiO_2 (3.0–3.2 eV) confines its photoactivity to the UV region ($\lambda \leq 400$ nm). The fast recombination of photogenerated electron-hole pairs in TiO_2 also reduces its photocatalytic efficiency [5–8].

To cope with the restrictions mentioned above, TiO_2 can be modified by metals, non-metals, and secondary semiconductors [9]. The incorporation of metals into TiO_2 can narrow its bandgap energy and prevent the recombination of electron-hole pairs, thereby improving the photocatalytic activity of TiO_2 for wastewater treatment applications [10]. This modification involves a variety of metals, including transition metals (e.g., Cr, Cu, Ni, Fe, V, W, Mn, Zn, and Ru), noble metals (e.g., Ag, Au, Pt, and Pd), and rare earth metals (e.g., Nd, Tb, Ce, Er, La, and Eu) [11]. Among these, composite Ag/TiO_2 photocatalysts have drawn research interest in wastewater treatment [12,13]. The presence of Ag in TiO_2 enhances its photocatalytic activity by reducing the recombination of photogenerated electron-hole pairs and improving visible light absorption [14–16].

Immobilizing photocatalysts on supports affects the stability and reusability of photoactive materials [10]. Porous polyurethane foam (PUF) is one of the floating supports, which has a low density (<1000 kg/m^3) [17,18]. PUF improves the adsorption of pollutants due to its

* Corresponding author. Department of Chemical Engineering, Polytechnique Montréal, Montréal, Canada.
E-mail address: daria-camilla.boffito@polymtl.ca (D.C. Boffito).

https://doi.org/10.1016/j.tgchem.2024.100059
Received 1 September 2024; Received in revised form 28 November 2024; Accepted 3 December 2024
Available online 4 December 2024

open-pore structure, which increases porosity and surface area [19]. In addition, photocatalysts deposited onto floating PUF tackle shortcomings such as the recovery and reusability of suspended photocatalysts, which hinder practical applications [19]. Moreover, the floating catalytic foam under sunlight irradiation benefits from access to the water-air interface [20]. This floating system causes a temperature gradient at the water-air interface, called the photothermal effect [21–23]. This attains the temperature-induced pumping effect and speeds up the mass transfer for photocatalysis [21]. The photothermal effect in the floating catalyst photoreactor also improves the absorption of oxygen from the air, enhancing photocatalytic reactions with increasing reactive oxygen species in the submerged part of floating photocatalysts in water [22].

Floating TiO_2-based photocatalysts have been explored for wastewater treatment. According to the literature, Zhang et al. [24] synthesized mesoporous SiO_2–TiO_2 photocatalysts supported on a floating polyurethane foam. Phenol and 2,4,5-trichlorophenol were completely removed by floating SiO_2–TiO_2/PUF after 3h and 6h under UV irradiation, respectively. TiO_2–ZnO photocatalysts immobilized on a floating light-expanded clay aggregate support (TiO_2–ZnO/LECA) were prepared by Mohammadi et al. [25], achieving 95.2 % of ammonia removal under UV light within 3h. Mohamad Idris et al. [26] fabricated floating photocatalysts, which were TiO_2 nanoparticles immobilized on cork as a floating substrate. This resulted in 98.4 % of methylene blue degradation after 2h of visible light. Cai et al. [27] described immobilizing co-doped magnetic N–TiO_{2-x}/rGO photocatalysts on floating cellulose nanofibrous. The floating N–TiO_{2-x}/rGO@cellulose degraded 96.2 % of Bisphenol A after 60 min under visible light. In another study, carbon and nitrogen co-doped TiO_2 nanoparticles supported on floating alginate beads were designed to remove diazinon [28]. The floating C, N–TiO_2/alginate bead removed 80.6 % of diazinon after 8h of exposure to solar light.

In the synthesis process of photocatalysts, ultrasonication assists in providing a uniform particle size distribution in photocatalysts through acoustic cavitation and macro shear rates [29,30]. This phenomenon consists of the fast formation, expansion, and intense collapse of bubbles in the liquid, leading to a high temperature (up to 5000 K) and pressure (20 MPa) and quick cooling rate [31–33]. In addition, the ultrasound-assisted impregnation method leads to the uniform distribution of photocatalysts onto their supports [34,35]. Besides ultrasonication, spray drying during the photocatalyst synthesis process provides a swift, continuous approach whereby lengthy drying steps are avoided. This technique is also advantageous when scaling up during the commercialization process [36,37]. Therefore, by applying ultrasonication and spray drying in subsequent steps during the synthesis of photoactive materials, we expect to enhance photocatalytic activity.

To the best of our knowledge, no study has been reported for the treatment of dye-containing wastewater using floating Ag/TiO_2 photocatalyst immobilized on porous PUF (Ag/TiO_2@PUF). We proposed a new synthesis process, i.e., an ultrasound-assisted sol-gel method followed by spray drying to manufacture a floating photocatalytic device. We compared the photocatalytic activity of suspended TiO_2 and Ag/TiO_2 with floating TiO_2@PUF and Ag/TiO_2@PUF to remove methyl orange (MO) as a model organic dye pollutant under simulated sunlight irradiation. In addition, we investigated the effects of operating parameters, including photocatalyst amount, MO concentration, and pH, on MO removal efficiency and kinetics study. Moreover, we examined the possible mechanism of MO removal by Ag/TiO_2@PUF and the main reactive species involved in the photocatalytic reaction under optimal conditions.

We hypothesized that floating TiO_2@PUF and Ag/TiO_2@PUF photocatalysts, inspired by photosynthesis, offer key advantages such as enhanced sunlight and oxygen harnessing over conventional suspended systems to remove MO at lower cost.

2. Materials and methods

2.1. Materials

Ti(IV)-butoxide ($C_{16}H_{36}O_4Ti$, 97 %) and methyl orange ($C_{14}H_{14}N_3NaO_3S$, 85 %) were analytical grade reagents purchased from Sigma-Aldrich. Ethanol (C_2H_6O, 95 %) was provided by Commercial Alcohols, and silver nitrate solution ($AgNO_3$, 0.1 N) was supplied by Merck. A commercial polyurethane foam (PUF, Porosity: Medium, 20 PPI) was obtained from Amtra (Italy). All solutions were prepared with deionized water, and the reagents were used as they were received without further purification.

2.2. Synthesis of photocatalysts

We synthesized pure TiO_2 and 2 wt% Ag-decorated TiO_2 by an ultrasound-assisted sol-gel method followed by spray drying. An ultrasonic processor (VCX500, Sonics and Materials) equipped with a solid probe with a diameter of 13 mm was employed (measured power: 40 W; duty cycle: 2 s on, 2 s off for 1 h; processing volume: 120 mL). The ultrasound power was calibrated through calorimetry [38]. The operating parameters of the spray dryer (TP-S15, TOPTION) included a feeding slurry concentration of 20 %, peristaltic pump feed rate of 30 rpm, temperature of 180 °C, and needle of 6 s. For the synthesis of Ag/TiO_2, we added $AgNO_3$ solution (5 mL) dropwise in deionized water (10 mL) to the mixture of $C_{16}H_{36}O_4Ti$ (25 mL) and ethanol (80 mL) under continuous ultrasonication [9,39]. After that, the resulting sol was fed to the spray dryer. The powder sample obtained from the spray dryer was then calcined in a furnace at 600 °C for 2 h at a temperature rate of 2 °C/min under static air, yielding Ag/TiO_2. TiO_2 was prepared using the same procedure without adding $AgNO_3$ solution.

The next step of the synthesis was to immobilize TiO_2 and Ag/TiO_2 onto a floating PUF by an ultrasound-assisted impregnation method. First, different amounts of TiO_2 and Ag/TiO_2 (0.5 g, 1 g, and 1.5 g) in deionized water were added to the PUF under continuous ultrasonication (40 W, 20 min). After that, ethanol (15 mL) was added to the solution, and the PUF was then immersed in the solution of deionized water and ethanol. Finally, the resulting solutions were dried at 80 °C for 24 h in the oven to obtain floating TiO_2@PUF and Ag/TiO_2@PUF.

2.3. Characterization

The crystalline phase of the synthesized photocatalysts was analyzed by a powder X-ray diffractometer (XRD, D8 advance, Bruker). Weight fractions of anatase and rutile phases were calculated by the Spurr Equation (Equation (1)), where I_R and I_A are the intensity of the strongest reflections for rutile and anatase phases [40].

$$f_A\,\% = \frac{1}{\left(1 + 1.26\,\frac{(I_R)}{(I_A)}\right)} \tag{1}$$

The crystallite size of the photocatalysts was calculated using the Scherrer Equation [41].

$$D = \frac{K\lambda}{\beta\,cos\,\theta} \tag{2}$$

In Equation (2), D is the crystallite size (nm), K is a constant (shape factor = 0.94), λ is the wavelength of the X-ray radiation source (Cu-Kα = 0.15406 nm), β is the full width at half maximum (FWHM) of the peak (in radian), and θ is half of the Bragg angle (in degrees).

The lattice parameters of the synthesized photocatalysts were determined with Bragg's law by the following equations [42] using XRD diffraction peaks of tetragonal TiO_2.

$$d_{(hkl)} = \frac{\lambda}{2\,sin\,\theta} \tag{3}$$

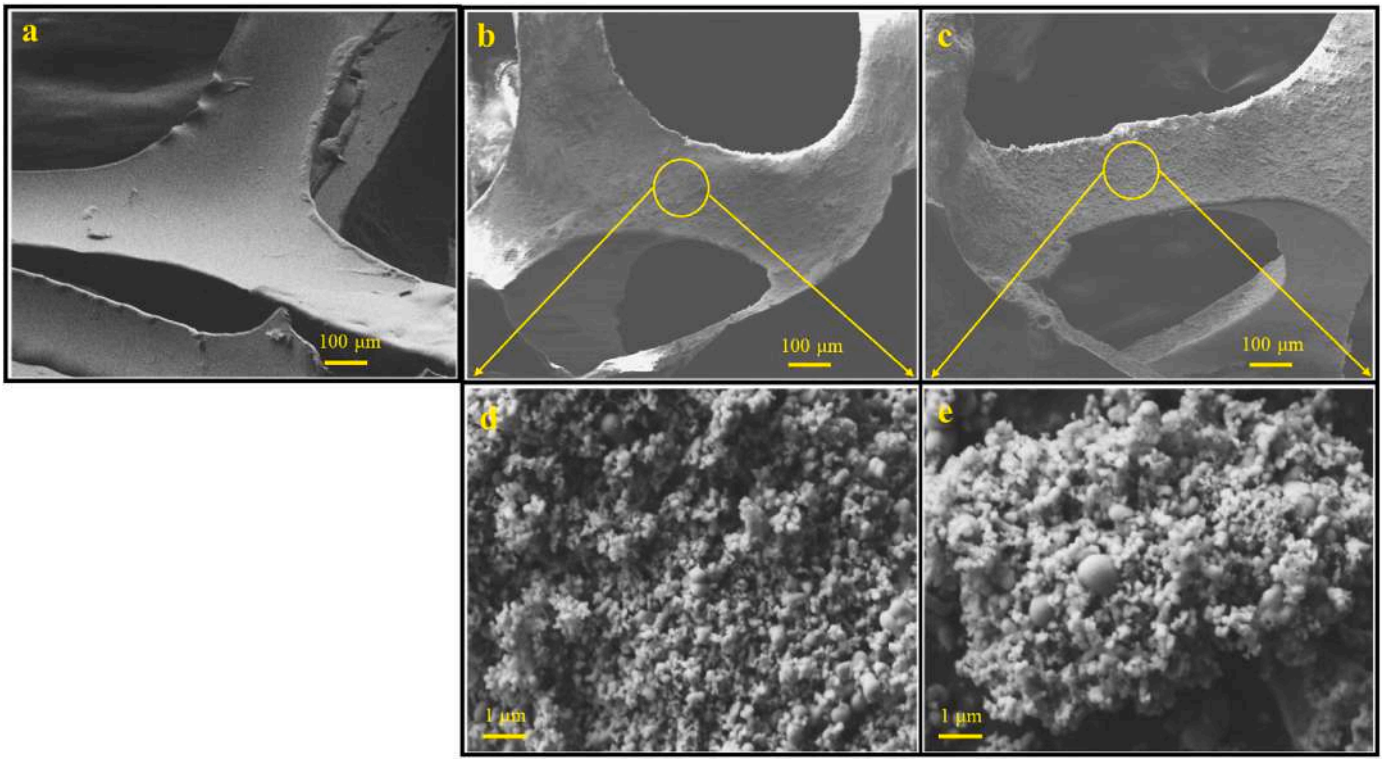

Fig. 1. SEM images of (a) PUF, (b) TiO_2@PUF, (c) Ag/TiO_2@PUF, (d) TiO_2, and (e) Ag/TiO_2.

$$\frac{1}{(d_{(hkl)})^2}=\frac{h^2}{a^2}+\frac{k^2}{b^2}+\frac{l^2}{c^2} \tag{4}$$

In Equations 3-4, h, k, l are the indices of crystal planes, $d_{(hkl)}$ is the distance between the crystal planes of (hkl), θ is the diffraction angle of the crystal planes of (hkl), and a, b, c are lattice parameters of the photocatalysts ($a = b \neq c$).

Diffuse reflectance spectroscopy (DRS) analysis was performed by a UV–Vis spectrophotometer (Evolution™ 220, Thermo Fisher Scientific) to study the optical properties of the synthesized photocatalysts. The bandgap energy of the photocatalysts was calculated by plotting $[F(R) \times h\upsilon]^{0.5}$ vs. $h\upsilon$ based on Equation (5) [41,43].

$$F(R)=\frac{(1-R)^2}{2R} \tag{5}$$

where $F(R)$ is the Kubelka Munk function, and R is the reflectance.

The infrared photothermal images of floating samples were taken by forward looking infrared camera (FLIR-T621xx). Scanning electron microscopy (SEM) equipped with energy-dispersive X-ray spectroscopy (EDS) was employed to investigate the morphology and elemental compositions of the photocatalysts (JSM-7600TFE, JEOL). Transmission electron microscopy (TEM) (JEM-2100F, JEOL) was operated to further study their morphology. Also, the size of the synthesized samples was measured using Digimizer version 5.3.5 software. For the chemical compositions and valence states of the photoactive materials, X-ray photoelectron spectroscopy (XPS) analysis was performed by an X-ray photoelectron spectrometer microprobe (VG ESCALAB 250Xi, Thermo Scientific). Nitrogen adsorption-desorption isotherms using the Brunauer-Emmett-Teller (BET) method measured the specific surface area, total pore volume, and pore size of the photocatalysts by an Autosorb-1 device (Quantachrome Instruments).

2.4. Photocatalytic system

We evaluated the photocatalytic activity of the synthesized materials to remove MO in a batch photoreactor under simulated sunlight irradiation. In addition, the stability of TiO_2, Ag/TiO_2, TiO_2@PUF, and Ag/TiO_2@PUF was assessed for five consecutive cycles. After each cycle, we removed the photocatalysts from the system, washed them with deionized water, and then dried them in the oven at 80 °C before reusing them for the next cycle. Each cycle had the same conditions.

We investigated the effect of operating parameters on MO removal with floating Ag/TiO_2@PUF under simulated sunlight irradiation as follows: Ag/TiO_2@PUF amount (0.2:200 g/mL, 0.4:200 g/mL, 0.8:200 g/mL), MO concentration (5 mg/L, 10 mg/L, 20 mg/L), and pH (4, 5.7, 10). The total irradiation time was 180 min, and the initial MO volume was 200 mL. Note that the values expressed for the photocatalysts as 0.2:200 g/mL, 0.4:200 g/mL, and 0.8:200 g/mL indicate the mass coated on PUF in the 200 mL of MO solution. The pH of MO solutions was adjusted by HCl (0.1 M) and NaOH (0.1 M), and the natural pH of the MO solution was measured at 5.7. In addition, the light source was a 300 W commercial solar lamp (Ultra-Vitalux, Osram) with an intensity of 35 W/m^2, located 20 cm above the reactor. Before being exposed to irradiation, each sample was kept in the dark for 60 min to reach absorption-desorption equilibrium. We repeated photocatalytic experiments three times under simulated sunlight irradiation, and error bars show the standard deviation of these repetitions. MO concentration was monitored by a UV–Vis spectrophotometer (Evolution™ 220, Thermo Fisher Scientific) at $\lambda_{max} = 464$ nm. The photocatalytic efficiency of MO removal (η) was calculated according to Equation (6):

$$\eta=\left(1-\frac{C}{C_0}\right)\times 100\% \tag{6}$$

where C_0 is the initial concentration of MO and C is the concentration of MO at time t.

We identified intermediates generated during the photocatalytic degradation of MO with floating Ag/TiO_2@PUF under optimal conditions using liquid chromatography-mass spectrometry (LC-MS). LC-UV-MS analyses were performed on an LC-TOF 6224 instrument from Agilent technologies with negative electrospray ionization.

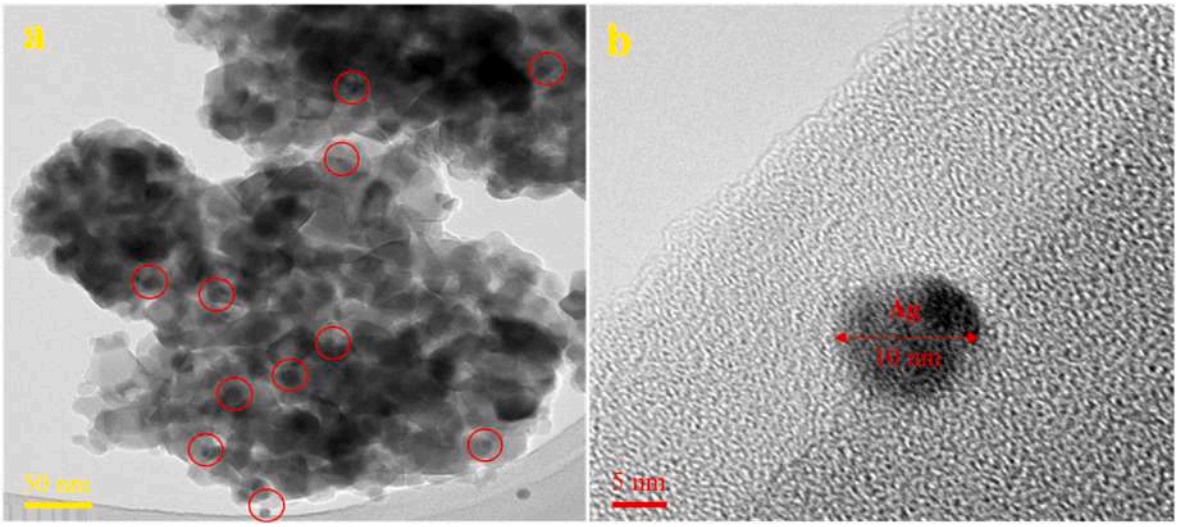

Fig. 2. TEM images of (a) Ag/TiO_2 and (b) Ag.

We quantified the concentration of Ti and Ag elements leaching from Ag/TiO_2@PUF using inductively coupled plasma-optical emission spectroscopy (ICP-OES, Agilent, 5110-SVDV).

2.5. Photocatalytic kinetic study

The impact of operating parameters mentioned in section 2.4 was also examined on the kinetic of MO photocatalysis with floating Ag/TiO_2@PUF under simulated sunlight irradiation. We followed the Langmuir-Hinshelwood kinetics model, as shown in Equation (7) [44].

$$r = \frac{dC}{dt} = \frac{kKC}{1 + KC} \tag{7}$$

r is the rate of MO removal (mg/L.min), C is MO concentration (mg/

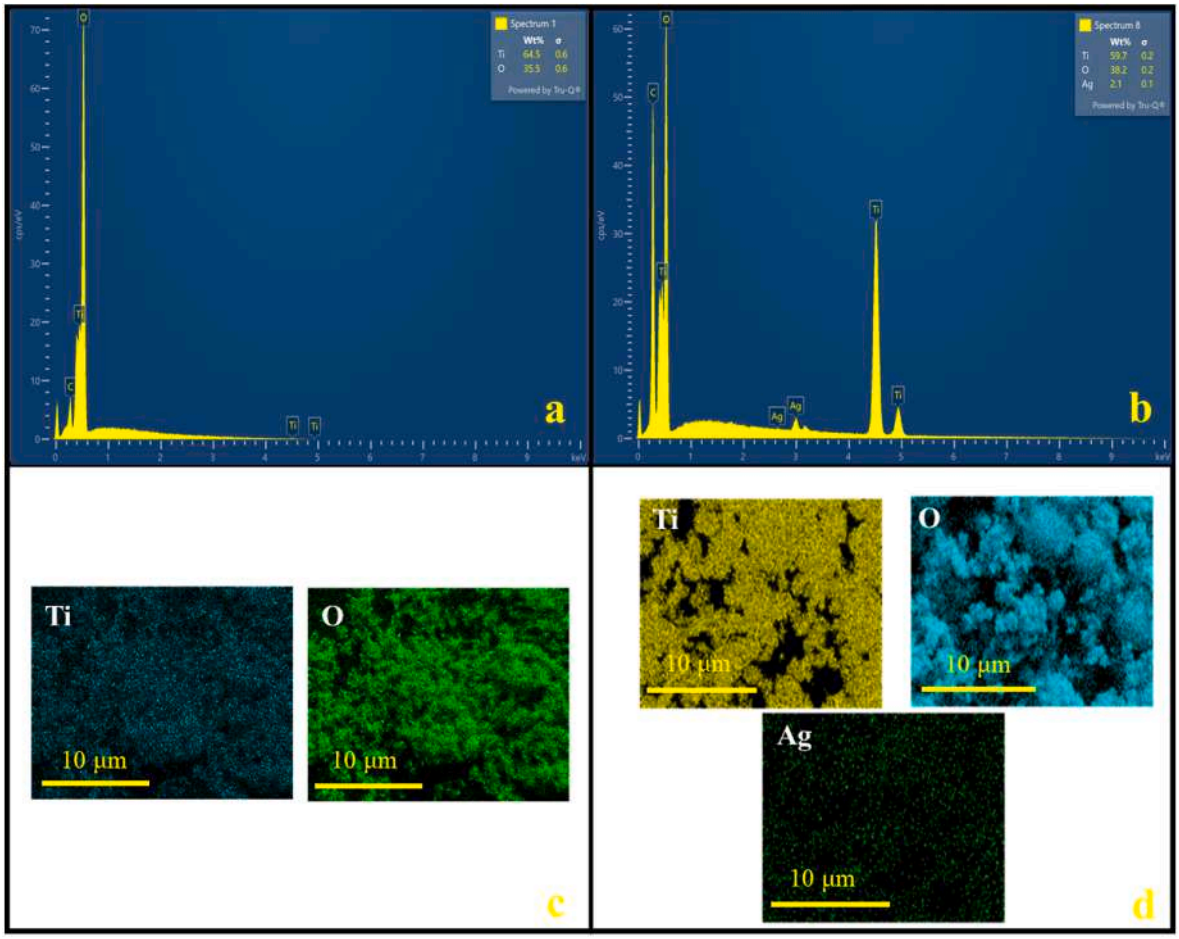

Fig. 3. EDS spectra of (a) TiO_2 and (b) Ag/TiO_2; EDS mappings of (c) TiO_2 and (d) Ag/TiO_2.

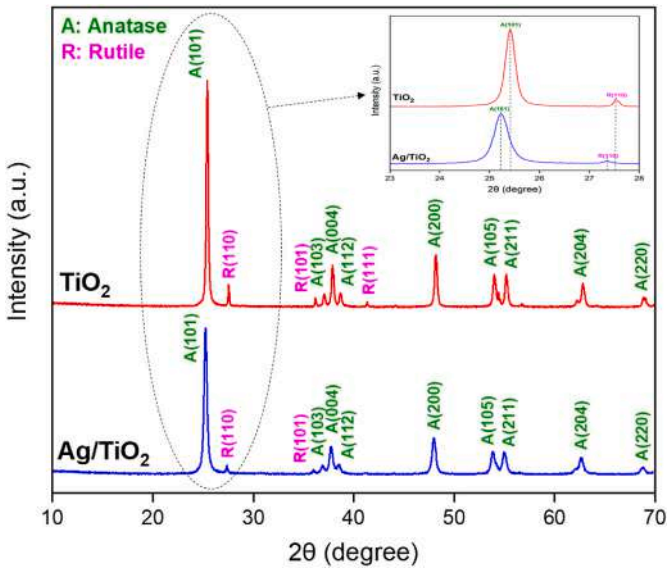

Fig. 4. XRD of TiO_2 and Ag/TiO_2.

L), t is irradiation time (min), k is reaction rate constant (mg/L.min), and K is MO adsorption constant (L/mg).

For low concentrations of MO, Equation (7) can be simplified to Equation (8), representing a first-order kinetics.

$$ln\left(\frac{C_0}{C}\right) = kKt = k_{app}t \quad (8)$$

In Equation (8), k_{app} is the apparent first-order rate constant (min^{-1}).

2.6. Scavenging experiments

We investigated the main reactive species involved in MO photocatalysis by floating Ag/TiO_2@PUF by adding the scavengers Ethylenediaminetetraacetic acid (EDTA), isopropyl alcohol (IPA), and *p*-benzoquinone (BQ) for photogenerated holes (h^+), hydroxyl radicals ($^{\bullet}OH$), and superoxide anions ($^{\bullet}O_2^-$), respectively. We added 1 mM of each scavenger to the floating catalyst photoreactor under simulated sunlight irradiation. We performed scavenging experiments for the optimized conditions of the photocatalysts in MO removal.

3. Results and discussion

3.1. Morphology and elemental compositions of TiO_2@PUF and Ag/TiO_2@PUF

Fig. 1a presents the smooth surface of the pristine PUF before immobilizing the photocatalysts. Fig. 1b and c shows the SEM images of TiO_2@PUF and Ag/TiO_2@PUF after the deposition of the photocatalysts, confirming that TiO_2 and Ag/TiO_2 were uniformly immobilized onto the PUF. This is due to ultrasonication in the impregnation synthesis method [35,45]. In addition, the synthesized TiO_2 and Ag/TiO_2 had spherical morphology, as depicted in Fig. 1d and e.

Fig. 2a shows the TEM image of Ag/TiO_2. Ag was uniformly loaded onto TiO_2, marked by highlighted circles. The size of spherical Ag was 10 nm, as shown in Fig. 2b.

EDS detected Ti (64.5 %) and O (35.5 %) in TiO_2 (Fig. 3a). Also, the presence of 2.1 % Ag in Ag/TiO_2 was confirmed, along with 59.7 % of Ti and 38.2 % of O in the photocatalyst (Fig. 3b). Fig. 3c and d shows that the elements were evenly dispersed onto the synthesized photocatalysts.

3.2. Crystalline phase of TiO_2 and Ag/TiO_2

Fig. 4 shows the XRD patterns of TiO_2 and Ag/TiO_2. The lattice planes of the anatase phase (101), (103), (004), (112), (200), (105), (211), (204), and (220) were confirmed at 2θ values of 25.47°, 37.15°, 37.97°, 38.78°, 48.21°, 54.04°, 55.22°, 62.87°, and 69.01°, respectively (JCPDS Card Number: 01-071-1166). Moreover, peaks at 2θ values of 27.60°, 36.22°, and 41.44° equivalent to the Miller indexes of (110), (101), and (111) were characteristic of the rutile phase in the synthesized photocatalysts (JCPDS Card Number: 00-001-1292). TiO_2-based photocatalysts having mixed phases (anatase/rutile) present higher photocatalytic activity compared to single-phase TiO_2 [46,47].

As shown in Fig. 4, the peak associated with Ag was not detected due to either the highly fine dispersion on TiO_2 or, more likely, the low concentration of Ag in Ag/TiO_2 [9]. However, for Ag/TiO_2, the position of TiO_2 peaks shifted to a lower angle side, and the intensity of peaks decreased, indicating that Ag was decorated on TiO_2 [48]. We calculated the crystalline phase, crystallite size, lattice parameters, and cell volume of TiO_2 and Ag/TiO_2 for both the anatase phase at A (101) and the rutile phase at R (110) (Table 1). Based on the Spurr Equation, TiO_2 had 88 % of the anatase phase compared to 92 % for Ag/TiO_2. According to the Scherrer Equation, the average crystallite size of anatase in TiO_2 was 32.8 nm and 26.5 nm for Ag/TiO_2. On the other hand, for the rutile phase, the crystallite size of TiO_2 and Ag/TiO_2 was 74.4 nm and 26.6 nm, respectively. The crystallite size of Ag/TiO_2 was smaller than that of pure TiO_2 due to the higher ionic radius of Ag^+ (126 Å) compared to Ti^{4+} (68 Å). This hinders the growth of TiO_2 crystallites [49]. As reported in Table 1, the lattice parameters of Ag/TiO_2 were smaller than those of TiO_2 in both anatase and rutile phases. Also, the anatase cell volume of Ag/TiO_2 was 132.16 $Å^3$ compared to 138.98 $Å^3$ for TiO_2. The reduction in lattice parameters and cell volume originates from Ag decoration on TiO_2 [48,50].

3.3. Chemical compositions and valence states of TiO_2 and Ag/TiO_2

Fig. 5a depicts the XPS survey spectra of TiO_2 and Ag/TiO_2, which indicates the presence of Ti and O in TiO_2 and Ti, O, and Ag elements for Ag/TiO_2. Ag/TiO_2 exhibited two peaks at binding energies of 458.8 eV for Ti $2p_{3/2}$ and 464.5 eV for Ti $2p_{1/2}$, indicating the existence of Ti^{4+} in Ag/TiO_2 based on the peak separation of 5.7 eV (Fig. 5b) [51–53]. In addition, there was about 0.1 eV shift in the Ti 2p spectrum of Ag/TiO_2 towards higher binding energy compared with TiO_2, which can result from the improved interaction between Ti and Ag [54]. Fig. 5c shows a peak at 530 eV attributed to the lattice oxygen in Ag/TiO_2 (Ti–O) [55,56]. In Fig. 5d, Ag 3d peaks were present at binding energies of 368.5 eV and 374.5 eV for Ag $3d_{5/2}$ and Ag $3d_{3/2}$, respectively. The binding energy difference between the two spin-orbit components was 6 eV, confirming the presence of metallic silver (Ag^0) in Ag/TiO_2 [51,53,57,58].

Table 1
Crystalline parameters of TiO_2 and Ag/TiO_2.

Photocatalyst	Crystalline phase	Crystalline phase percentage	Crystallite size (nm)	Lattice parameters (Å)		Cell volume ($Å^3$)
				a = b	c	
TiO_2	Anatase	88	32.8	3.7917	9.6672	138.98
Ag/TiO_2		92	26.5	3.7746	9.2756	132.16
TiO_2	Rutile	12	74.4	4.6113	2.9712	63.18
Ag/TiO_2		8	26.6	4.5695	2.9528	61.65

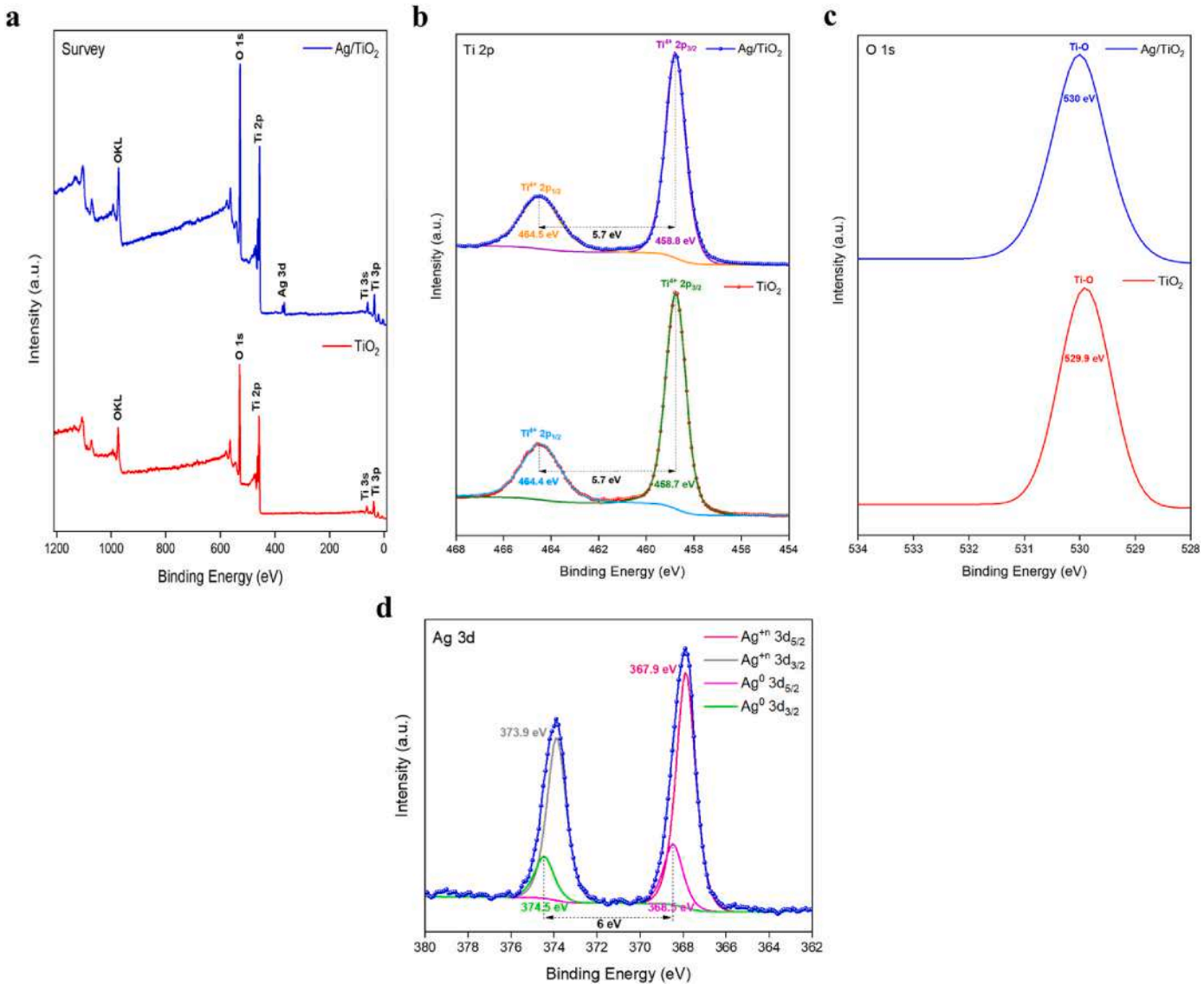

Fig. 5. XPS spectra of TiO_2 and Ag/TiO_2 (a) Full spectrum, (b–d) High-resolution spectra of Ti 2p, O 1s, and Ag 3d, respectively.

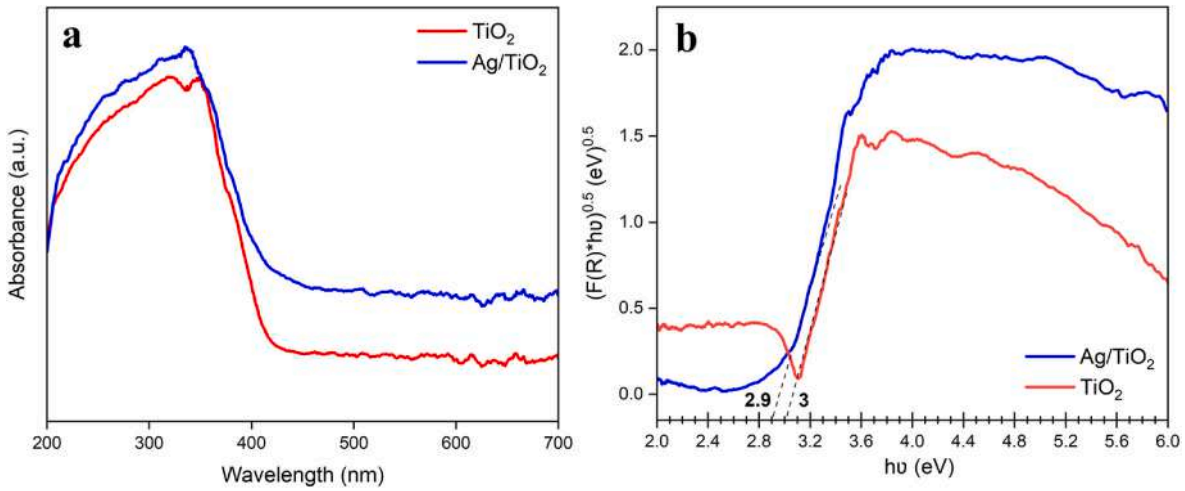

Fig. 6. DRS (a) absorption spectra and (b) Tauc plots of TiO_2 and Ag/TiO_2.

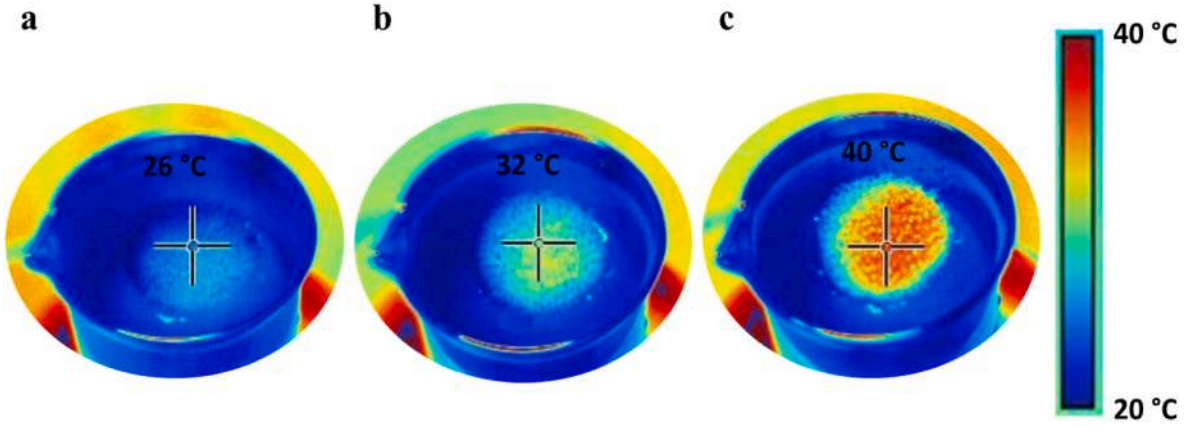

Fig. 7. Top-view infrared photothermal images of (a) PUF, (b) TiO_2@PUF, and (c) Ag/TiO_2@PUF in water under simulated sunlight irradiation.

Table 2
BET of TiO_2 and Ag/TiO_2.

Photocatalyst	BET surface area (m^2/g)	Pore volume (cm^3/g)	Pore size (nm)
TiO_2	10	0.03	12
Ag/TiO_2	30	0.12	10

Additional binding energy peaks were observed at 367.9 eV for Ag $3d_{5/2}$ and 373.9 eV for Ag $3d_{3/2}$, suggesting the presence of oxidized silver, either as Ag_2O or AgO (Ag^{+1} or Ag^{+2}) in the surface of TiO_2 [29,53,55,57,59,60]. The presence of oxidized silver is likely due to the oxidation of Ag during the calcination of Ag/TiO_2 [29]. Our results confirmed that Ag existed in Ag/TiO_2 as a mixture of metallic and oxidized silver.

3.4. Optical features and photothermal performance of TiO_2 and Ag/TiO_2

Fig. 6a presents the absorption spectra of TiO_2 and Ag/TiO_2. Pure TiO_2 exhibited an intense absorption peak in the UV region below 400 nm, which belongs to the electron excitation from the 2p of O^{2-} to the 3d orbital of Ti^{4+} [42]. According to Fig. 6a, a redshift towards 470 nm was observed in the spectrum of Ag/TiO_2 compared to bare TiO_2. This redshift can be due to the effect of Ag decoration on TiO_2, which improves the visible light absorption of TiO_2 [14,61].

Fig. 6b shows Tauc plots of TiO_2 and Ag/TiO_2. The bandgap energy of pure TiO_2 was determined as 3 eV. Ag decreased the bandgap energy of TiO_2 to 2.9 eV owing to decorating Ag on TiO_2 [15]. A new energy level can be formed between the conduction band of TiO_2 and the conduction band of Ag that decreases the bandgap energy of TiO_2, reducing the recombination rate of photogenerated charge carriers and thus enhancing the photocatalytic activity of Ag/TiO_2 [29,50].

Fig. 7 shows the infrared photothermal images of floating samples. The system reached the highest temperature at 26 °C, 32 °C and 40 °C for PUF, TiO_2@PUF and Ag/TiO_2@PUF, respectively, after 5 min of simulated sunlight irradiation. Ag/TiO_2@PUF exhibited the highest temperature of all samples (40 °C), which can be due to the local surface plasmon resonance (LSPR) effect of Ag [23,61]. Ag can generate high-energy hot electrons, resulting in local heating around the particles under light irradiation [62].

3.5. Textural properties of TiO_2 and Ag/TiO_2

Table 2 presents BET results of TiO_2 and Ag/TiO_2. BET surface area of Ag/TiO_2 (30 m^2/g) was three times higher than that of TiO_2 (10 m^2/g). In addition, Ag/TiO_2 had a total pore volume of 0.12 cm^3/g, four times greater than TiO_2 (0.03 cm^3/g).

Fig. 8a and b shows N_2 adsorption-desorption isotherms of TiO_2 and Ag/TiO_2, respectively. Based on the IUPAC classification [63], TiO_2 presented a type IV(a) isotherm with an H3 hysteresis loop, indicating its mesoporous geometry with a mean pore size of 12 nm (see Table 2). In addition, Ag/TiO_2 had a type IV(a) isotherm with an H1 hysteresis loop, suggesting a narrow range of uniform mesopores in Ag/TiO_2 and a mean

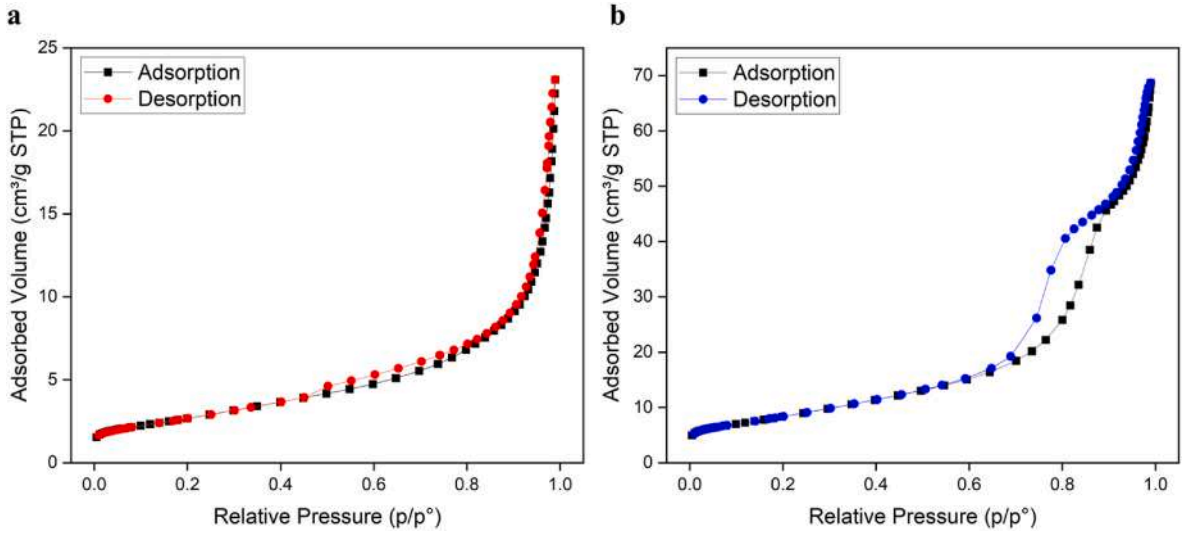

Fig. 8. N_2 adsorption-desorption isotherms of (a) TiO_2 and (b) Ag/TiO_2.

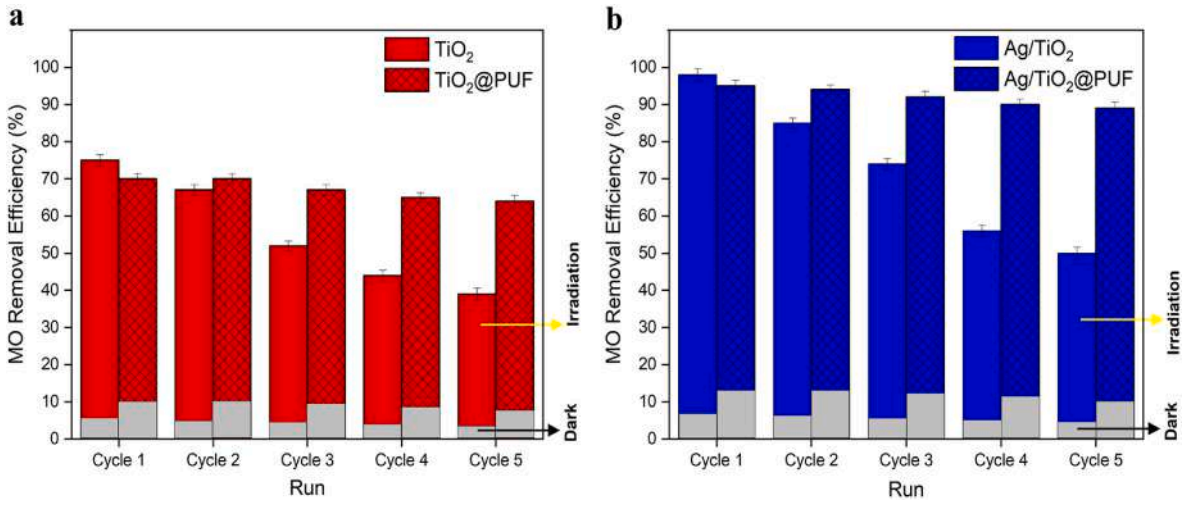

Fig. 9. MO removal efficiency with (a) TiO_2 and TiO_2@PUF, (b) Ag/TiO_2 and Ag/TiO_2@PUF after 180 min of irradiation time.

pore size of 10 nm.

3.6. Photocatalytic activity of TiO_2 and Ag/TiO_2 in suspended and floating systems for MO removal

We investigated suspended and floating devices based on TiO_2 and Ag/TiO_2 to remove MO under simulated sunlight irradiation for five consecutive cycles. The experimental conditions for MO photocatalysis were 10 mg/L of MO concentration, 0.4 g of photocatalysts, and pH = 5.7 for 180 min irradiation time. In the first cycle, the MO removal was 75 % and 70 % for TiO_2 and TiO_2@PUF, respectively (Fig. 9a). This slightly higher efficiency by suspended TiO_2 (5 %) can be attributed to the larger surface in contact with the MO solution, which is typical of suspensions, improving the mass transfer rate between the surface of TiO_2 nanoparticles and pollutant species [64–66]. On the other hand, in the second cycle, floating TiO_2@PUF maintained 70 % of MO removal, while it decreased to 67 % for suspended TiO_2. This reduction can be due to the loss of TiO_2 in the suspended form during its reuse [64]. In addition, floating TiO_2@PUF showed higher photocatalytic activity than suspended TiO_2 in the fifth cycle, achieving 64 % MO removal compared to 39 %. Immobilizing powder photocatalysts onto floating supports not only addresses the challenges of reuse of suspended photocatalysts but also enhances solar light harnessing through access to the water-air interface [67,68].

Fig. 9b presents the MO removal with Ag/TiO_2 and Ag/TiO_2@PUF in suspension and floating systems, respectively. Fig. 9b followed the same trend as observed in Fig. 9a. In the first cycle, suspended Ag/TiO_2 removed 98 % of MO, while Ag/TiO_2@PUF achieved 95 %. In the following cycles, floating Ag/TiO_2@PUF exhibited higher photocatalytic activity than suspended Ag/TiO_2. The MO removal was 89 % with floating Ag/TiO_2@PUF and 50 % for suspended Ag/TiO_2 in the final cycle. Comparing Fig. 9b with Fig. 9a, Ag in both suspended and floating photocatalysts increased the MO removal with respect to the pure photocatalysts. Our results indicated that floating Ag/TiO_2@PUF was the most effective photocatalyst, with a MO removal efficiency of 89 % after five consecutive cycles. Based on the results from Ag/TiO_2@PUF characterizations, Ag decoration on TiO_2 decreased the bandgap energy to 2.9 eV and caused an increase in the visible light absorption of bare TiO_2 [14,23]. Also, the surface area of Ag/TiO_2 increased to 30 m^2/g, three times higher than that of TiO_2, providing more active sites for the decomposition of MO. In addition, the mixed phase found for Ag/TiO_2 exhibited higher photocatalytic activity than the single-phase one [46,47].

Floating photocatalysts (TiO_2@PUF and Ag/TiO_2@PUF) were 5–7% more effective than suspended ones (TiO_2 and Ag/TiO_2) in adsorbing MO in dark conditions. This is because the floating photocatalytic

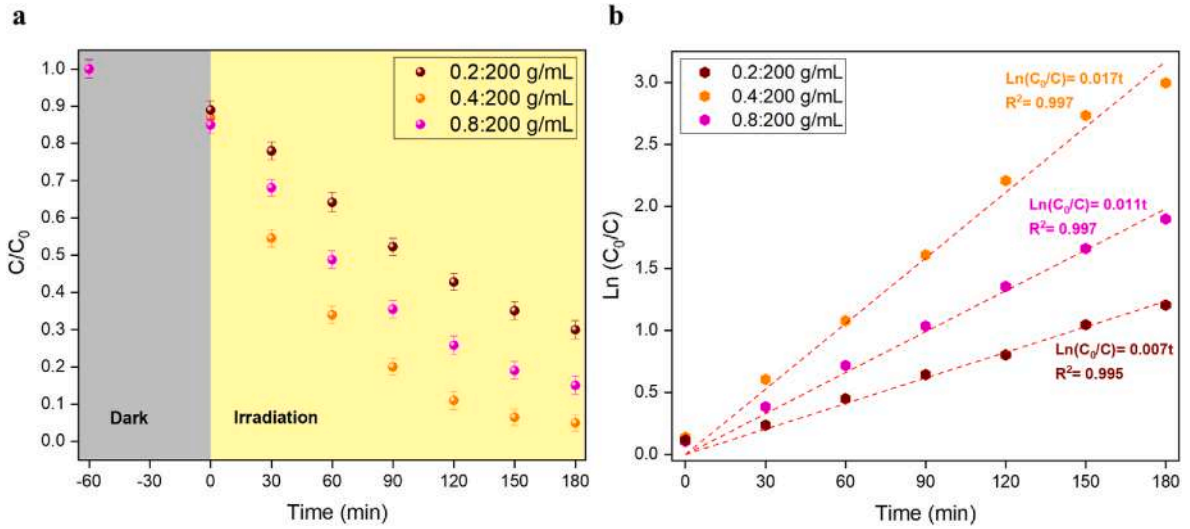

Fig. 10. Effect of Ag/TiO_2@PUF amount (0.2:200 g/mL, 0.4:200 g/mL, 0.8:200 g/mL) on (a) MO removal efficiency and (b) apparent rate constant.

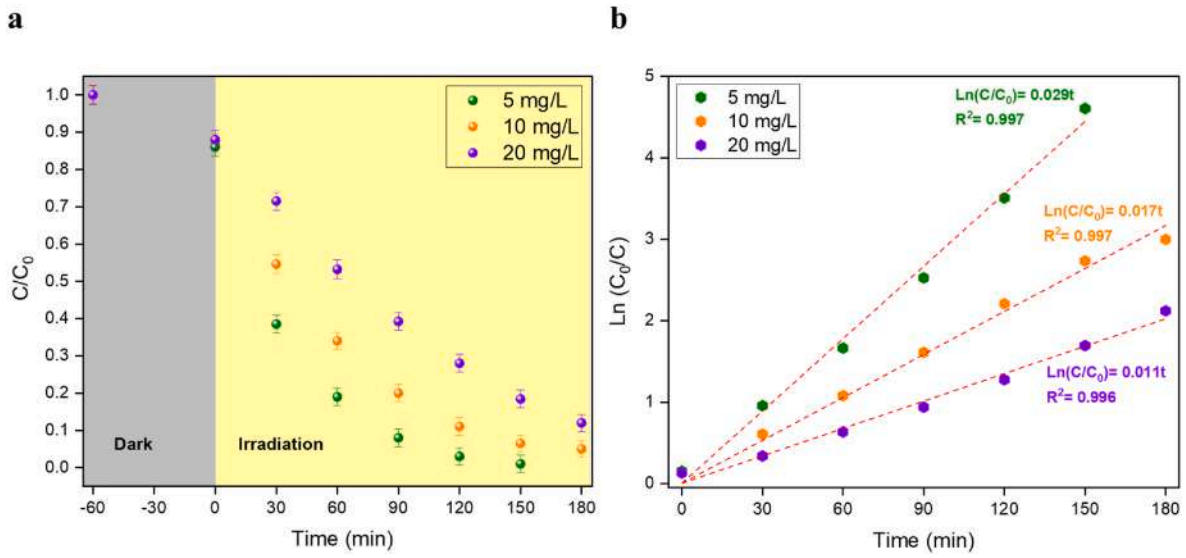

Fig. 11. Effect of MO concentration (5 mg/L, 10 mg/L, 20 mg/L) on (a) MO removal efficiency and (b) apparent rate constant.

systems benefit from the photothermal effect [21–23,61] that enhances the diffusion and adsorption of MO molecules on the surface of floating photocatalysts during the photocatalytic process.

3.7. Effects of operating parameters on MO removal by floating Ag/TiO_2@PUF

The effect of Ag/TiO_2@PUF amount on MO removal efficiency under simulated sunlight irradiation was investigated by varying it to 0.2:200 g/mL, 0.4:200 g/mL, and 0.8:200 g/mL. The rest of the experimental conditions were maintained constant (pH = 5.7, 10 mg/L MO, and 180 min irradiation time). Fig. 10a shows that when the photocatalyst amount increased from 0.2:200 g/mL to 0.4:200 g/mL, the MO removal rose from 70 % to 95 %. This increase is because more active photocatalytic sites inside the PUF can be available to harness light irradiation and participate in the photocatalytic reaction [18]. On the other hand, the MO removal decreased by 10 % with increasing amount of the photocatalyst from 0.4:200 g/mL to 0.8:200 g/mL due to the agglomeration of Ag/TiO_2 and blockage of PUF pores that hinder light penetration [18,69–71]. Our results suggested that the optimal amount of Ag/TiO_2@PUF for MO photocatalysis was 0.4:200 g/mL, achieving 95 % removal after 180 min.

Fig. 10b presents the effect of Ag/TiO_2@PUF amount on the apparent rate constant. The correlation coefficients (R^2) were higher than 0.98, confirming that the MO photocatalytic removal by Ag/TiO_2@PUF followed first-order kinetics. As shown in Fig. 10b, by increasing the amount of Ag/TiO_2@PUF from 0.2:200 g/mL to 0.4:200 g/mL, the apparent first-order rate constant (k_{app}) increased from 0.007 min^{-1} to 0.017 min^{-1}. However, as the amount of Ag/TiO_2@PUF further raised to 0.8:200 g/mL, k_{app} diminished to 0.011 min^{-1}.

The effect of MO concentration (5 mg/L, 10 mg/L, and 20 mg/L) on the MO removal was examined with 0.4:200 g/mL Ag/TiO_2@PUF at pH = 5.7. For Mo concentration of 5 mg/L, we observed a complete removal after 150 min of irradiation time (Fig. 11a). However, increasing the MO concentration to 10 mg/L decreased the efficiency to 95 % after 180 min, and it was 93 % for 150 min. In addition, a further increase in MO concentration to 20 mg/L resulted in a 7 % reduction in the MO removal (see Fig. 11a). The results showed that the photocatalytic performance of Ag/TiO_2@PUF decreased by increasing the MO concentration. This can be owing to the large adsorption of MO on the photocatalyst surface, decreasing the photodecomposition efficiency [72,73]. The MO photocatalytic removal was affected by the initial pollutant concentration in

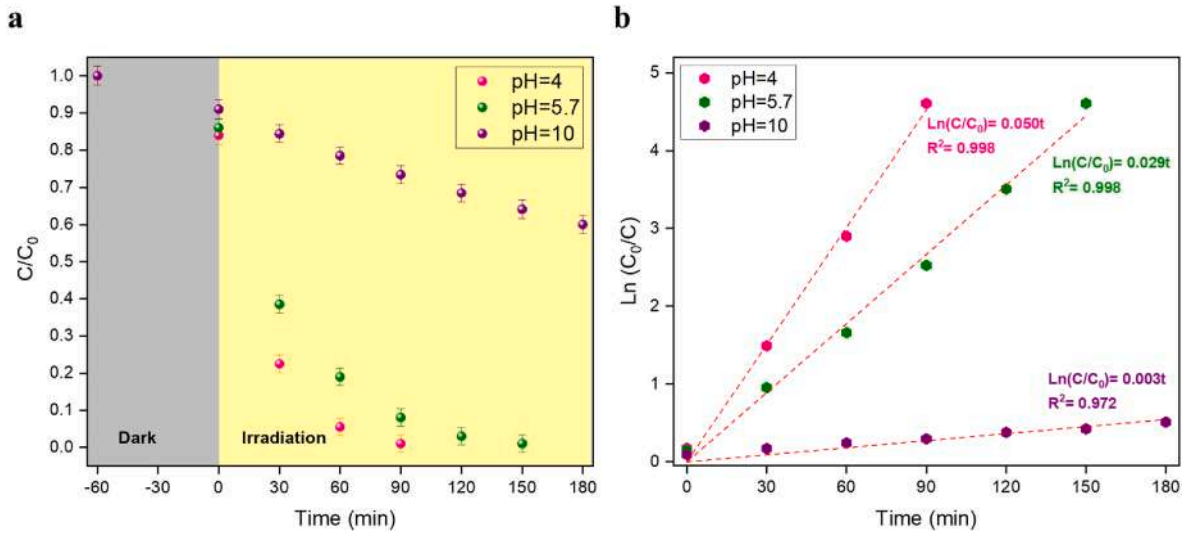

Fig. 12. Effect of pH (4, 5.7, 10) on (a) MO removal efficiency and (b) apparent rate constant.

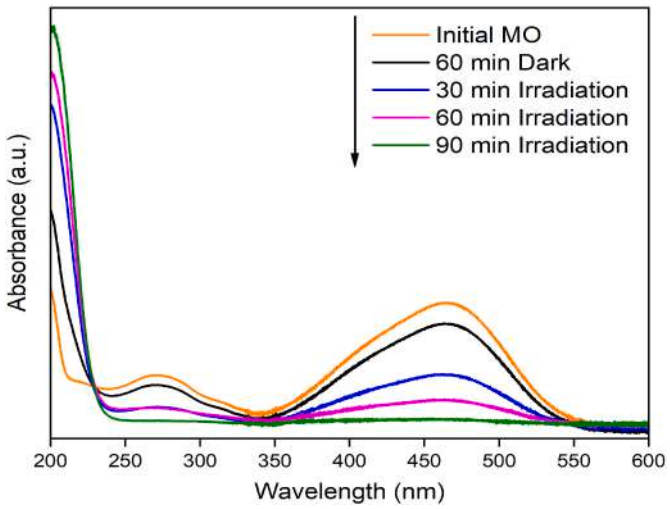

Fig. 13. UV–Vis absorption spectra of MO removal under the optimal conditions (MO concentration = 5 mg/L, Ag/TiO_2@PUF amount = 0.4:200 g/mL, pH = 4, and irradiation time = 90 min).

which complete elimination was achieved for 5 mg/L MO after 150 min.

Fig. 11b shows how the concentration of MO impacts the apparent rate constant in the MO photocatalytic process. When applying Ag/TiO_2@PUF for MO removal, the system obeyed first-order kinetics, with R^2 exceeding 0.99. Also, rising MO concentration from 5 mg/L to 20 mg/L lowered k_{app} from 0.029 min^{-1} to 0.011 min^{-1}.

The effect of pH on MO removal was also evaluated. We tested the pH of MO solution (4, 5.7, and 10) using 5 mg/L MO and 0.4:200 g/mL Ag/TiO_2@PUF. Fig. 12a shows that as the pH of the MO solution decreases, the removal efficiency increases. The lowest MO removal rate happened at pH = 10 (40 % after 180 min), which can be explained by the surface charge properties of Ag/TiO_2@PUF. The point of zero charge for TiO_2 is 6 (pH_{PZC} = 6) [15,44,74]. Thus, the surface of TiO_2 in Ag/TiO_2@PUF is negatively charged at pH = 10, as presented in Equation (9).

$$TiOH + OH^- \leftrightarrow TiO^- + H_2O \quad (9)$$

On the other hand, MO is an anionic dye with a pk_a of 3.4 [44], which is negatively charged at pH = 10. Consequently, electrostatic repulsion between the negatively charged MO and the negatively charged surface of Ag/TiO_2@PUF [15,44] inhibits the adsorption of MO onto the photocatalyst, decreasing the photocatalytic efficiency. In addition, at pH = 5.7, the surface of TiO_2 in Ag/TiO_2@PUF is positively charged according to Equation (10), while MO is negatively charged [15,44].

$$TiOH + H^+ \leftrightarrow TiOH_2^+ \quad (10)$$

Therefore, there is an electrostatic attraction between the negatively charged pollutant and the positively charged surface of the photocatalyst [15,44] that favours the adsorption of MO onto the photocatalyst and thus increases MO removal. MO was completely removed at pH = 5.7 after 150 min of irradiation time. Moreover, MO removal was predominant at pH = 4, achieving complete removal after 90 min of light irradiation (see Fig. 12a). The improved photocatalytic activity of Ag/TiO_2@PUF at pH = 4 compared to pH = 5.7 can be attributed to the pH_{PZC} of TiO_2 (pH_{PZC} = 6). At pH = 4, the surface of TiO_2 in Ag/TiO_2@PUF is strongly positively charged with a zeta potential value of around +30 mV [75,76], while it is about +5 mV at pH = 5.7 [75,76]. Consequently, the surface of Ag/TiO_2@PUF at pH = 4 is more positively charged to adsorb negatively charged MO and increases the removal efficiency. Our findings indicated that MO (5 mg/L) at pH = 4 was completely removed by Ag/TiO_2@PUF (0.4:200 g/mL) under simulated sunlight irradiation (90 min).

Fig. 12b shows the effect of pH on the apparent rate constant, suggesting that MO removal by Ag/TiO_2@PUF followed a first-order kinetics. At pH = 4, k_{app} was 0.050 min^{-1}, which was the highest value obtained for this system.

The faster removal rate for MO occurred at the beginning of the photocatalytic reaction due to the high initial concentration of MO.

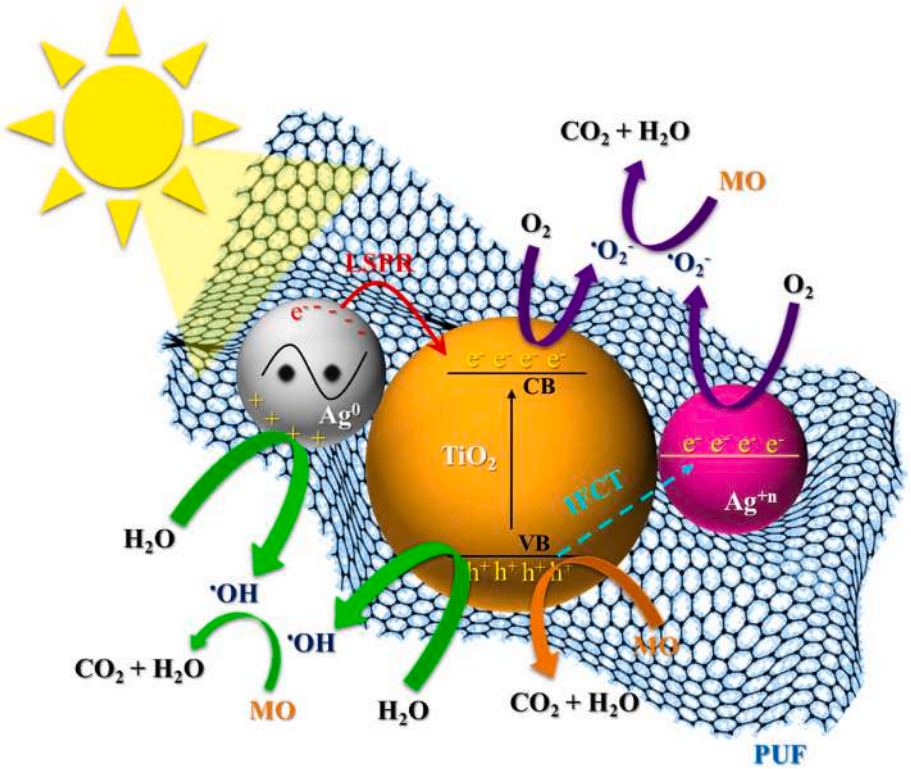

Fig. 14. Schematic of the possible mechanism for MO removal with Ag/TiO_2@PUF under simulated sunlight irradiation.

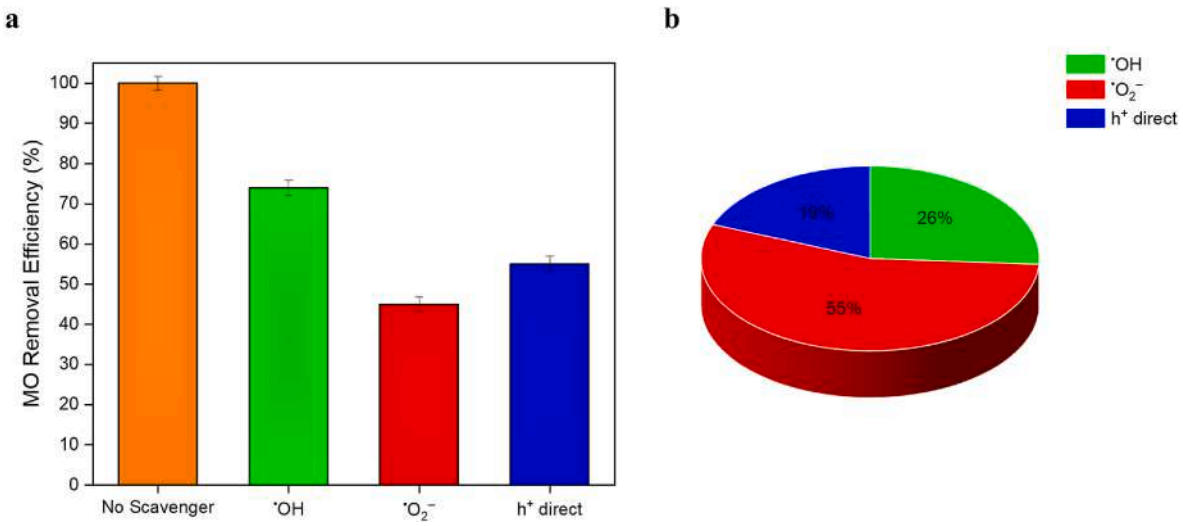

Fig. 15. (a) Free radical scavenging experiments and (b) reactive species contribution on MO removal using Ag/TiO_2@PUF under optimal conditions.

Based on the Langmuir-Hinshelwood kinetics model ($-r_A = k_{app}C_A$), the reaction rate was directly proportional to the concentration of MO. Therefore, at the start of the photocatalytic reaction, MO has its maximum concentration, resulting in a higher reaction rate. As the reaction proceeds, MO concentration decreases over time, which reduces the reaction rate.

Fig. 13 shows the UV–Vis absorption spectra of MO removal under the optimal conditions: MO concentration = 5 mg/L, Ag/TiO_2@PUF amount = 0.4:200 g/mL, pH = 4, and irradiation time = 90 min. The maximum absorption peak of MO was observed at 464 nm, which decreased to nearly zero during 90 min irradiation time. This suggests the potential cleavage of the azo group (–N=N–) in the MO structure [77], resulting in the complete removal of MO after 90 min. In addition, we investigated ICP-OES analysis for the leaching of Ti and Ag elements from Ag/TiO_2@PUF during MO removal under optimal conditions. According to the results, Ti and Ag were not observed (limit of detection of 0.000028 ppm for Ti and 0.0007 ppm for Ag) in the solution, suggesting that the metals were not released from the photocatalyst.

3.8. Possible mechanism of MO removal by Ag/TiO_2@PUF

We proposed the possible mechanism of photocatalytic MO removal using Ag/TiO_2@PUF under simulated sunlight irradiation (Fig. 14). According to Equation (11), electrons in the valence band (VB) of TiO_2 were excited by simulated solar light and then migrated to the conduction band (CB) of TiO_2, creating positively charged holes in the VB and negatively charged electrons in the CB of TiO_2. From the XPS results, Ag existed on the surface of TiO_2 as Ag^0. At the same time, the metallic silver absorbed sunlight irradiation and created hot electrons by means of the LSPR effect (Equation (12)) [14,78,79]. The creation of hot electrons corresponded to forming Ag^+, which participated in an oxidation reaction to produce $^\bullet$OH (Equation (13)). The hot electrons of Ag^0 had more negative energy than the CB of TiO_2 (−0.5 V vs. NHE [80]), so they migrated to the CB of TiO_2 and reacted with oxygen to form $^\bullet O_2^-$ (Equation (14)). In addition, oxidized silver (Ag_2O or AgO) was present in the photocatalyst surface, which can contribute to removing MO. Ag^{+n} (Ag^{+1} or Ag^{+2}) had more positive band energy (0.8 V vs. NHE [81]) than TiO_2. Under sunlight irradiation, excited electrons from the VB of TiO_2 moved to Ag^{+n} by interfacial charge transfer (IFCT) [54,79]. The IFCT improves the separation of electron-hole pairs and contributes to MO removal by generating reactive oxygen species [54]. The existing electrons in the CB of TiO_2 and Ag^{+n} participated in the reduction reaction and converted O_2 to $^\bullet O_2^-$ (Equation (14)). Consequently, the presence of Ag in TiO_2 not only improves the photoinduced charge generation but also suppresses the electron-hole pairs recombination [15,16,79]. Simultaneously, the photoinduced holes on the VB of TiO_2 participated in an oxidation reaction and converted H_2O into $^\bullet$OH (Equation (15)). Eventually, the generated reactive species (i.e., $^\bullet O_2^-$ and $^\bullet$OH) can react with MO and convert it into CO_2 and H_2O (Equations (16) and (17)). Moreover, as shown in Equation (18), the photoinduced holes on the VB of TiO_2 can convert MO into CO_2 and H_2O directly.

$$TiO_2 + h\nu \rightarrow h_{VB}^+ + e_{CB}^- \quad (11)$$

$$Ag^0 + h\nu \rightarrow Ag^+ + e^- \quad (12)$$

$$Ag^+ + H_2O \rightarrow {}^\bullet OH + H^+ \quad (13)$$

$$e_{CB}^- + O_2 \rightarrow {}^\bullet O_2^- \quad (14)$$

$$h_{VB}^+ + H_2O \rightarrow {}^\bullet OH + H^+ \quad (15)$$

$$^\bullet O_2^- + MO \rightarrow CO_2 + H_2O \quad (16)$$

$$^\bullet OH + MO \rightarrow CO_2 + H_2O \quad (17)$$

$$h_{VB}^+ + MO \rightarrow CO_2 + H_2O \quad (18)$$

Fig. 15a shows free radical scavenging experiments performed under optimal conditions to evaluate the contribution of each reactive species to the photocatalytic MO removal. Fig. 15a shows that adding BQ as a $^\bullet O_2^-$ scavenger decreased MO removal from 100 % to 45 %, indicating a 55 % reduction in the removal efficiency by $^\bullet O_2^-$. In addition, 55 % of MO was removed in the presence of EDTA as a h^+ scavenger. To determine the direct and indirect contributions of h^+, IPA as a $^\bullet$OH scavenger was added to the floating system, causing a 26 % reduction in the MO removal. Thus, h^+ had a 19 % contribution to remove MO directly and the contribution of $^\bullet$OH was 26 %. Also, $^\bullet O_2^-$ was the main reactive species in MO removal with a 55 % contribution, as depicted in Fig. 15b.

Fig. 16a shows the LC-MS chromatograms for the photocatalytic degradation of MO under optimal conditions (MO concentration = 5 mg/L, Ag/TiO_2@PUF amount = 0.4:200 g/mL, pH = 4, and irradiation time = 90 min). Initially, a strong peak was observed at m/z = 304, which belongs to MO. After 30 min of degradation, the MO peak decreased, while some new peaks appeared, which were attributed to the degradation products of MO. After 60 min, all the peaks gradually decreased and finally disappeared at 90 min. Fig. 16b depicts

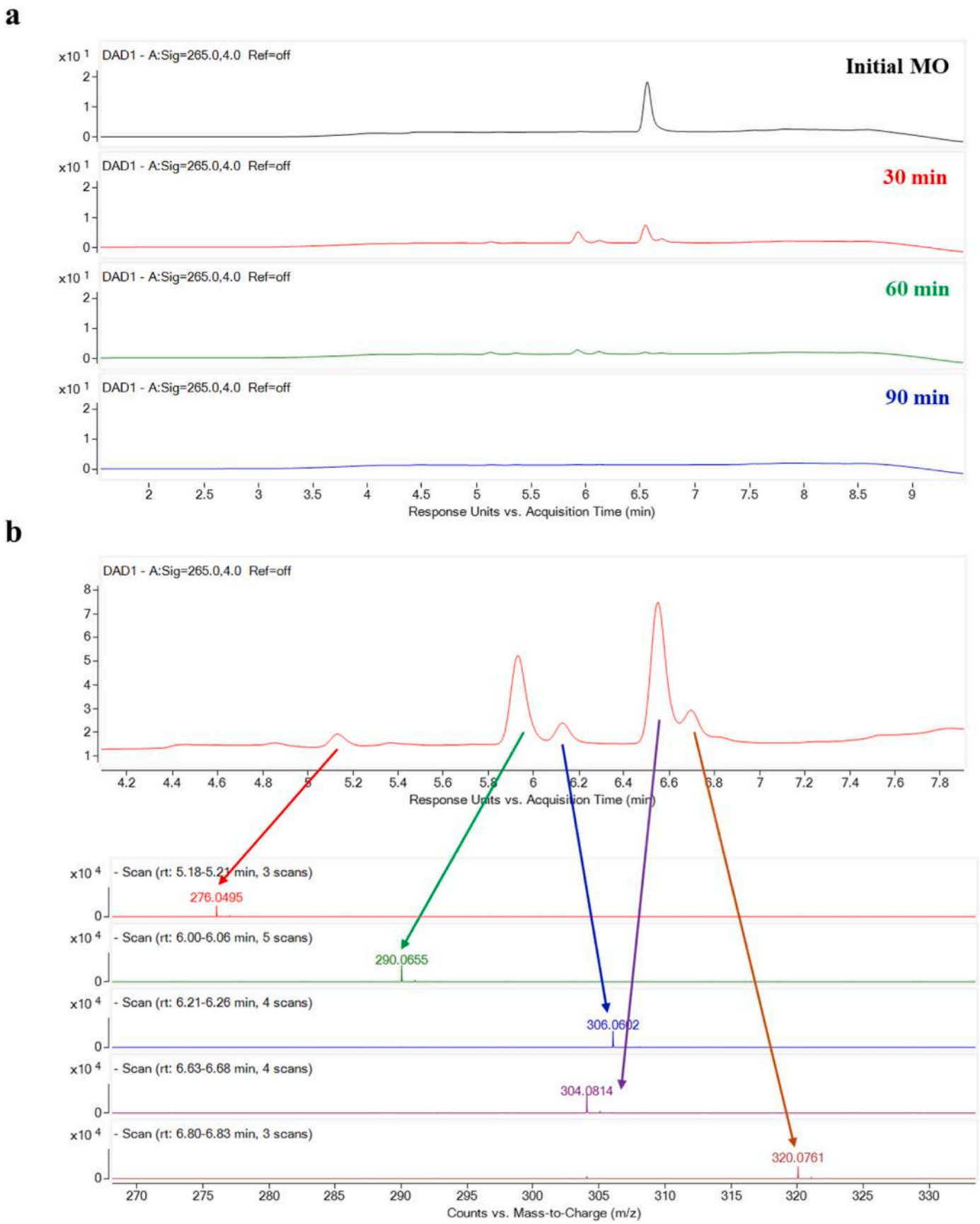

Fig. 16. (a) LC-MS chromatograms of MO degradation for 0 min, 30 min, 60 min, and 90 min under optimal conditions and (b) identified intermediates from MO degradation after 30 min.

Table 3
Recent literature review on the photocatalytic removal of MO.

Photocatalytic system	Photocatalyst	Synthesis method	Pollutant	Reaction time	Removal efficiency	Kinetics	Ref.
Floating	g-C_3N_4 on PUF (30 mg/L)	Thermal decomposition and dip coating	MO (5 mg/L)	240 min (LED lamp)	75.1 %	Pseudo first-order ($k = 0.0032\ min^{-1}$)	[72]
Suspension	Fe_3O_4/GO (0.150 g/40 mL)	Co-precipitation, modified Hummers, and ultrasonication	MO (10 mg/L)	240 min (UV light)	99 %	NA	[88]
Suspension	g-C_3N_4/ZnO (2 g/L)	Thermal polycondensation	MO (NA)	120 min (Solar light)	98 %	NA	[89]
Suspension	TiO_2/biochar (6 g/L)	High-temperature pyrolysis, sol-gel, and ultrasonic-assisted vacuum impregnation	MO (50 mg/L)	270 min (Xenon lamp)	97.9 %	Pseudo first-order ($k = 0.00769\ min^{-1}$)	[87]
Suspension	Sn-doped TiO_2 (0.5 g/L)	Microwave-assisted sol-gel	MO (1×10^{-5} M)	180 min (UV light)	94 %	NA	[90]
Floating	Ag/TiO_2@PUF (0.4:200 g/mL)	Ultrasound-assisted sol-gel followed by spray drying and ultrasound-assisted impregnation	MO (5 mg/L)	90 min (Simulated sunlight)	100 %	First-order ($k = 0.050\ min^{-1}$)	Present work

intermediates generated after 30 min of MO degradation, with identified peaks at $m/z = 320$, 306, 290 and 276. The intermediate compounds of $m/z = 320$ and $m/z = 306$ are related to the monohydroxylated product of MO and the oxidation in the aromatic ring of MO, respectively [82]. Also, the detected compounds with $m/z = 290$ and $m/z = 276$ correspond to demethylated products of MO [83,84]. According to the literature, further photocatalytic degradation of MO can lead to the mineralization of these intermediates, forming CO_2 and H_2O [83–86].

3.9. Comparison of floating Ag/TiO_2@PUF for MO removal with previous work

Table 3 reports a comparison of the present work with other recent studies for the photocatalytic removal of MO. Based on Table 3, only one study utilized a floating photocatalytic system for MO removal. Swathi et al. [72] synthesized floating g-C_3N_4 photocatalysts supported on PUF, removing 75.1 % of MO after 240 min of irradiation. In another study [87], the removal efficiency of MO was 97.9 % by suspended TiO_2/-biochar photocatalysts after 270 min based on pseudo first-order kinetics. In this work, our floating Ag/TiO_2@PUF photocatalyst was efficient in eliminating MO after 90 min of simulated sunlight irradiation.

4. Conclusion

We fabricated suspended and floating TiO_2 and Ag/TiO_2 photocatalysts using an ultrasound-assisted sol-gel method, followed by spray drying to remove MO. The results showed the uniform deposition of the photocatalysts onto the floating PUF due to the ultrasonication in the impregnation synthesis method. The decoration of Ag on TiO_2 extends its absorption into the visible-light range. Ag/TiO_2 had a mixed-phase, and its BET surface area increased to 30 m^2/g, which was three times higher than TiO_2. The existence of Ag in TiO_2 for both suspended and floating systems increased MO removal efficiency. Floating Ag/TiO_2@-PUF had more photocatalytic activity than suspended Ag/TiO_2, removing 89 % of MO after five consecutive cycles. In addition, MO was completely removed with Ag/TiO_2@PUF under optimal conditions as MO concentration = 5 mg/L, photocatalyst amount = 0.4:200 g/mL, pH = 4, and irradiation time = 90 min (300 W commercial solar lamp with an intensity of 35 W/m^2). Moreover, MO removal by Ag/TiO_2@PUF followed first-order kinetics ($k_{app,\ Maximum} = 0.050\ min^{-1}$), and the main reactive species involved in MO removal was $^{\bullet}O_2^-$ (55 %). Our results suggest that Ag/TiO_2@PUF constitutes a promising approach to removing coloured organic pollutants from wastewater. Due to the photocatalytic properties of Ag/TiO_2@PUF, we suggest applying this floating photocatalyst to treat other aqueous organic pollutants. Future work can focus on either modifying the elemental composition of the photocatalyst or adding oxidants like H_2O_2 to decrease the activation energy for the MO removal and consequently decrease the degradation process time.

Editorial disclosure statement

Daria C. Boffito is an editorial board member and had no involvement in the peer-review of this article and has no access to information regarding its peer-review. Full responsibility for the editorial process for this article was delegated to Editor, Giovanni Poli.

CRediT authorship contribution statement

Nila Davari: Writing – original draft, Visualization, Validation, Methodology, Investigation, Formal analysis, Data curation, Conceptualization. **Ermelinda Falletta:** Writing – review & editing, Methodology, Investigation, Data curation. **Claudia L. Bianchi:** Writing – review & editing, Project administration, Methodology, Investigation, Funding acquisition, Data curation. **Viviane Yargeau:** Writing – review & editing, Supervision, Project administration, Methodology, Investigation, Data curation. **Cristina Rodriguez-Seco:** Writing – review & editing. **Daria C. Boffito:** Writing – review & editing, Supervision, Resources, Project administration, Methodology, Investigation, Funding acquisition, Data curation.

Declaration of competing interest

The authors declare that they have no known competing financial interests or personal relationships that could have appeared to influence the work reported in this paper.

Acknowledgments

The authors thank the Velux Stiftung Foundation for the financial support through project 1381, “SUNFLOAT - Water decontamination by sunlight-driven floating photocatalytic systems”. We also appreciate the support of Bourse d’excellence Neil R. Mitchell et Danièle Dumais.

Data availability

Data will be made available on request.

References

[1] Z. Huang, H. Liu, Insights into the pathways, intermediates, influence factors and toxicological properties in the degradation of tetracycline by TiO2-based photocatalysts, J. Environ. Chem. Eng. 11 (5) (2023) 110587, https://doi.org/10.1016/j.jece.2023.110587.
[2] S.N. Sadikin, J. Ridwan, M.I.A. Umar, A.A.M. Raub, J. Yunas, A.A. Hamzah, et al., Photocatalytic activity and stability properties of porous TiO2 film as photocatalyst

for methylene blue and methylene orange degradation, Int. J. Electrochem. Sci. 18 (9) (2023) 100246, https://doi.org/10.1016/j.ijoes.2023.100246.
[3] S.G. Hosseini, J.V. Pasikhani, Enhanced optical properties and photocatalytic activity of TiO2 nanotubes by using magnetic activated carbon: evaluating photocatalytic reduction of Cr(VI), Environ. Technol. 42 (6) (2021) 914–931, https://doi.org/10.1080/09593330.2019.1649466.
[4] N. Gilani, J. Vahabzadeh Pasikhani, M. Akbari, P. Tafazoli Motie, Hydrogen evolution from catalytic hydrolysis of NaBH4: Comparative study between the catalytic activity of TiO2 nanotubes with various arrangements, J Journal of Nanostructures 9 (3) (2019) 587–599, https://doi.org/10.22052/jns.2019.03.020.
[5] T.M. Pham, K.Q. Bui, D.V. Le, H.Q. Pham, T.T. Huynh, T.M. Ngo, et al., Visible Light-Driven N–F-Codoped TiO2 for Photocatalysts as Potential Application to Wastewater Treatment 46 (5) (2023) 865–872, https://doi.org/10.1002/ceat.202200388.
[6] F.D. Ali, S.H. Ammar, N.D. Ali, Y.R. Abdulmajeed, Z.H. Jabbar, Synthesis of AgCl/ZIF-8/C–TiO2 heterojunction photocatalysts for enhanced degradation of levofloxacin under visible-light, Mater. Sci. Semicond. Process. 172 (2024) 108100, https://doi.org/10.1016/j.mssp.2023.108100.
[7] R. Habibi, N. Gilani, J.V. Pasikhani, A.E. Pirbazari, Improved photoelectrocatalytic activity of anodic TiO2 nanotubes by boron in situ doping coupled with geometrical optimization: application of a potent photoanode in the purification of dye wastewater, J. Solid State Electrochem. 25 (2) (2021) 545–560, https://doi.org/10.1007/s10008-020-04825-6.
[8] M. Hajiali, M. Farhadian, S. Aflaki, N. Davari, Application of TiO2/ZnFe2O4/glycine nanocatalyst to the treatment of methyl orange dye from aqueous solution: impacts of dissolved mineral salts on dye removal efficiency %J Scientia Iranica, Sci. Iran. 28 (3) (2021) 1464–1477, https://doi.org/10.24200/sci.2021.56415.4715.
[9] A. Sabir, T.A. Sherazi, Q. Xu, Porous polymer supported Ag-TiO2 as green photocatalyst for degradation of methyl orange, Surface. Interfac. 26 (2021) 101318, https://doi.org/10.1016/j.surfin.2021.101318.
[10] D. Kanakaraju, F.D. anak Kutiang, Y.C. Lim, P.S. Goh, Recent progress of Ag/TiO2 photocatalyst for wastewater treatment: doping, co-doping, and green materials functionalization, Appl. Mater. Today 27 (2022) 101500, https://doi.org/10.1016/j.apmt.2022.101500.
[11] D. Jiang, T.A. Otitoju, Y. Ouyang, N.F. Shoparwe, S. Wang, A. Zhang, et al., A review on metal ions modified TiO2 for photocatalytic degradation of organic pollutants 11 (9) (2021) 1039, https://doi.org/10.3390/catal11091039.
[12] Q. Zhang, D. Thrithamarassery Gangadharan, Y. Liu, Z. Xu, M. Chaker, D. Ma, Recent advancements in plasmon-enhanced visible light-driven water splitting, Journal of Materiomics 3 (1) (2017) 33–50, https://doi.org/10.1016/j.jmat.2016.11.005.
[13] Q. Zhang, J. Deng, Z. Xu, M. Chaker, D. Ma, High-efficiency broadband C3N4 photocatalysts: synergistic effects from upconversion and plasmons, ACS Catal. 7 (9) (2017) 6225–6234, https://doi.org/10.1021/acscatal.7b02013.
[14] J. Jia, S. Giannakis, D. Li, B. Yan, T. Lin, Efficient and sustainable photocatalytic inactivation of E. coli by an innovative immobilized Ag/TiO2 photocatalyst with peroxymonosulfate (PMS) under visible light, Sci. Total Environ. 901 (2023) 166376, https://doi.org/10.1016/j.scitotenv.2023.166376.
[15] M. Rehan, E. Elhaddad, An efficient multi-functional ternary reusable nanocomposite based on chitosan@TiO2@Ag NP immobilized on cellulosic fiber as a support substrate for wastewater treatment, Environ. Pollut. 340 (2024) 122850, https://doi.org/10.1016/j.envpol.2023.122850.
[16] T.Z. Liza, M.M.H. Tusher, F. Anwar, M.F. Monika, K.F. Amin, F.N.U. Asrafuzzaman, Effect of Ag-doping on morphology, structure, band gap and photocatalytic activity of bio-mediated TiO2 nanoparticles, Results in Materials 22 (2024) 100559, https://doi.org/10.1016/j.rinma.2024.100559.
[17] L. Zhang, Z. Xing, H. Zhang, Z. Li, X. Zhang, Y. Zhang, et al., Multifunctional Floating Titania-Coated Macro/Mesoporous Photocatalyst for Efficient Contaminant Removal 80 (3) (2015) 623–629, https://doi.org/10.1002/cplu.201402327.
[18] L. Ni, Y. Li, C. Zhang, L. Li, W. Zhang, D. Wang, Novel floating photocatalysts based on polyurethane composite foams modified with silver/titanium dioxide/graphene ternary nanoparticles for the visible-light-mediated remediation of diesel-polluted surface water 133 (19) (2016), https://doi.org/10.1002/app.43400.
[19] L.S. Mendieta-Rodríguez, L.M. González-Rodríguez, J.J. Alcaraz-Espinoza, A. E. Chávez-Guajardo, J.C. Medina-Llamas, Synthesis and characterization of a polyurethane-polyaniline macroporous foam material for methyl orange removal in aqueous media, Mater. Today Commun. 26 (2021) 102155, https://doi.org/10.1016/j.mtcomm.2021.102155.
[20] N. Davari, E. Falletta, C.L. Bianchi, V. Yargeau, D.C. Boffito, TiO2 nanotubes immobilized on polyurethane foam as a floating photocatalyst for water treatment, Catal. Today 436 (2024) 114725, https://doi.org/10.1016/j.cattod.2024.114725.
[21] Z. Zhang, L. Zhang, Z. Huang, Y. Xu, Q. Zhao, H. Wang, et al., "Floating Catalytic Foam" with prominent heat-induced convection for the effective photocatalytic removal of antibiotics, J. Hazard Mater. 463 (2024) 132879, https://doi.org/10.1016/j.jhazmat.2023.132879.
[22] S. Zhang, R. Wang, K. Wang, M. Wang, Z. He, H. Chen, et al., Aeration-free in situ fenton-like reaction: specific adsorption and activation of oxygen on heterophase oxygen vacancies, Environ. Sci. Technol. 58 (4) (2024) 1921–1933, https://doi.org/10.1021/acs.est.3c08579.
[23] L. Ren, W. Zhou, L. Wang, K. Lin, Y. Xu, J. Wu, et al., All-in-one self-floating porous foams as robust heat-blocking layers for efficient photothermal conversion and solar desalination, Sci. Bull. 68 (22) (2023) 2760–2768, https://doi.org/10.1016/j.scib.2023.08.062.
[24] L. Zhang, Z. Xing, H. Zhang, Z. Li, X. Wu, X. Zhang, et al., High thermostable ordered mesoporous SiO2–TiO2 coated circulating-bed biofilm reactor for unpredictable photocatalytic and biocatalytic performance, Appl. Catal. B Environ. 180 (2016) 521–529, https://doi.org/10.1016/j.apcatb.2015.07.002.
[25] Z. Mohammadi, S. Sharifnia, Y. Shavisi, Photocatalytic degradation of aqueous ammonia by using TiO2ZnO/LECA hybrid photocatalyst, Mater. Chem. Phys. 184 (2016) 110–117, https://doi.org/10.1016/j.matchemphys.2016.09.031.
[26] Idris NH. Mohamad, J. Rajakumar, K.Y. Cheong, B.J. Kennedy, T. Ohno, A. Yamakata, et al., Titanium dioxide/polyvinyl alcohol/cork nanocomposite: a floating photocatalyst for the degradation of methylene blue under irradiation of a visible light source, ACS Omega 6 (22) (2021) 14493–14503, https://doi.org/10.1021/acsomega.1c01458.
[27] Y. Cai, Y. Chen, S. Ge, X. Qu, N. Sheng, L. Yang, et al., Co-doped magnetic N-TiO2-x/rGO heterojunction@cellulose nanofibrous flakelet for enhanced photocatalytic oxidation and facile separation: efficient charge separation and self-floatability, Chem. Eng. J. 425 (2021) 131462, https://doi.org/10.1016/j.cej.2021.131462.
[28] Idris NH. Mohamad, K.Y. Cheong, S.M. Smith, H.L.C. Lee, N-codoped TiO2 nanoparticles immobilized on floating alginate beads for diazinon removal under solar light irradiation, ACS Appl. Nano Mater. 7 (16) (2024) 18273–18286, https://doi.org/10.1021/acsanm.3c03622.
[29] M. Stucchi, C.L. Bianchi, C. Argirusis, V. Pifferi, B. Neppolian, G. Cerrato, et al., Ultrasound assisted synthesis of Ag-decorated TiO2 active in visible light, Ultrason. Sonochem. 40 (2018) 282–288, https://doi.org/10.1016/j.ultsonch.2017.07.016.
[30] M. Stucchi, A. Elfiad, M. Rigamonti, H. Khan, D.C. Boffito, Water treatment: Mn-TiO2 synthesized by ultrasound with increased aromatics adsorption, Ultrason. Sonochem. 44 (2018) 272–279, https://doi.org/10.1016/j.ultsonch.2018.01.023.
[31] J.S. Jeyaprakash, M. Rajamani, P. Mani, C. Yazhini, S.H. Sonawane, B. Neppolian, Highly efficient ultrasound-driven Ti3+-doped TiO2 with oxygen vacancies: a promising visible-light catalyst for complete sonophotocatalytic degradation of tetracycline, Ind. Eng. Chem. Res. 63 (12) (2024) 5135–5147, https://doi.org/10.1021/acs.iecr.3c04429.
[32] X. Xiong, Y. Shang, L. Bai, S. Luo, T.W. Seviour, Z. Guo, et al., Complete defluorination of perfluorooctanoic acid (PFOA) by ultrasonic pyrolysis towards zero fluoro-pollution, Water Res. 235 (2023) 119829, https://doi.org/10.1016/j.watres.2023.119829.
[33] W.L. Ang, P.J. McHugh, M.D. Symes, Sonoelectrochemical processes for the degradation of persistent organic pollutants, Chem. Eng. J. 444 (2022) 136573, https://doi.org/10.1016/j.cej.2022.136573.
[34] S. Manickam, D. Camilla Boffito, E.M.M. Flores, J.-M. Leveque, R. Pflieger, B. G. Pollet, et al., Ultrasonics and sonochemistry: Editors' perspective, Ultrason. Sonochem. 99 (2023) 106540, https://doi.org/10.1016/j.ultsonch.2023.106540.
[35] V.K. Landge, S.H. Sonawane, S. Manickam, G.U. Bhaskar Babu, G. Boczkaj, Ultrasound-assisted wet-impregnation of Ag–Co nanoparticles on cellulose nanofibers: enhanced catalytic hydrogenation of 4-nitrophenol, J. Environ. Chem. Eng. 9 (4) (2021) 105719, https://doi.org/10.1016/j.jece.2021.105719.
[36] H. Khan, M.G. Rigamonti, G.S. Patience, D.C. Boffito, Spray dried TiO2/WO3 heterostructure for photocatalytic applications with residual activity in the dark, Appl. Catal. B Environ. 226 (2018) 311–323, https://doi.org/10.1016/j.apcatb.2017.12.049.
[37] H. Khan, M.G. Rigamonti, D.C. Boffito, Enhanced photocatalytic activity of Pt-TiO2/WO3 hybrid material with energy storage ability, Appl. Catal. B Environ. 252 (2019) 77–85, https://doi.org/10.1016/j.apcatb.2019.04.019.
[38] D. Meroni, R. Djellabi, M. Ashokkumar, C.L. Bianchi, D.C. Boffito, Sonoprocessing: from concepts to large-scale reactors, Chem. Rev. 122 (3) (2022) 3219–3258, https://doi.org/10.1021/acs.chemrev.1c00438.
[39] Z. Khani, D. Schieppati, C.L. Bianchi, D.C. Boffito, The sonophotocatalytic degradation of pharmaceuticals in water by MnOx-TiO2 systems with tuned band-gaps 9 (11) (2019) 949, https://doi.org/10.3390/catal9110949.
[40] M. Mokhtarifar, R. Kaveh, M. Bagherzadeh, A. Lucotti, M. Pedeferri, M. V. Diamanti, Heterostructured TiO2/SiO2/γ-Fe2O3/rGO coating with highly efficient visible-light-induced self-cleaning properties for metallic artifacts, ACS Appl. Mater. Interfaces 12 (26) (2020) 29671–29683, https://doi.org/10.1021/acsami.0c06792.
[41] N. Davari, M. Farhadian, A.R.S. Nazar, M. Homayoonfal, Degradation of diphenhydramine by the photocatalysts of ZnO/Fe2O3 and TiO2/Fe2O3 based on clinoptilolite: structural and operational comparison, J. Environ. Chem. Eng. 5 (6) (2017) 5707–5720, https://doi.org/10.1016/j.jece.2017.10.052.
[42] J.V. Pasikhani, B.G. Aliabadi, N. Gilani, A.E. Pirbazari, Construction of NiO and Ti3 + self-doped TNTs thin film as a high quantum yield p-n type heterojunction via a novel photoelectrodeposition-assisted anodization method, J. Photochem. Photobiol. Chem. 418 (2021) 113433, https://doi.org/10.1016/j.jphotochem.2021.113433.
[43] N. Davari, M. Farhadian, A.R. Solaimany Nazar, Synthesis and characterization of Fe2O3 doped ZnO supported on clinoptilolite for photocatalytic degradation of metronidazole, Environ. Technol. 42 (11) (2021) 1734–1746, https://doi.org/10.1080/09593330.2019.1680738.
[44] M.V. Roldán, E. Porta, A. Durán, Y. Castro, N. Pellegri, Development of photocatalysts based on TiO2 films with embedded Ag nanoparticles. 13 (3) (2022) 429–443, https://doi.org/10.1111/ijag.16575.
[45] R.K. Polagani, M.A. Devani, G.U.B. Babu, M. Chinthala, K.N. Dhanavath, S. H. Sonawane, Ultrasound assisted impregnation of platinum on carbon for ORR activity in PEM fuel cell, Int. J. Ambient Energy 43 (1) (2022) 8239–8247, https://doi.org/10.1080/01430750.2022.2092776.
[46] P. Apopei, C. Catrinescu, C. Teodosiu, S. Royer, Mixed-phase TiO2 photocatalysts: crystalline phase isolation and reconstruction, characterization and photocatalytic activity in the oxidation of 4-chlorophenol from aqueous effluents, Appl. Catal. B

Environ. 160–161 (2014) 374–382, https://doi.org/10.1016/j.apcatb.2014.05.030.
[47] D.R. Eddy, M.D. Permana, L.K. Sakti, G.A.N. Sheha, Hidayat S. Solihudin, et al., Heterophase Polymorph of TiO2 (anatase, rutile, Brookite, TiO2 (B)) for efficient photocatalyst: fabrication and activity 13 (4) (2023) 704, https://doi.org/10.3390/nano13040704.
[48] R. Senthil Kumar, B. Gnanavel, High performance catalytic activity of pure and silver (Ag) doped TiO2 nanoparticles by a novel microwave irradiation technique, J. Mater. Sci. Mater. Electron. 28 (5) (2017) 4253–4259, https://doi.org/10.1007/s10854-016-6048-2.
[49] A. Sirivallop, T. Areerob, S. Chiarakorn, Enhanced visible light photocatalytic activity of N and Ag doped and Co-doped TiO2 synthesized by using an in-situ solvothermal method for gas phase ammonia removal 10 (2) (2020) 251, https://doi.org/10.3390/catal10020251.
[50] T. Ali, A. Ahmed, U. Alam, I. Uddin, P. Tripathi, M. Muneer, Enhanced photocatalytic and antibacterial activities of Ag-doped TiO2 nanoparticles under visible light, Mater. Chem. Phys. 212 (2018) 325–335, https://doi.org/10.1016/j.matchemphys.2018.03.052.
[51] Y. Zhang, F. Fu, Y. Li, D. Zhang, Y. Chen, One-step synthesis of Ag@TiO2 nanoparticles for enhanced photocatalytic performance 8 (12) (2018) 1032, https://doi.org/10.3390/nano8121032.
[52] M. Xu, Y. Wang, J. Geng, D. Jing, Photodecomposition of NOx on Ag/TiO2 composite catalysts in a gas phase reactor, Chem. Eng. J. 307 (2017) 181–188, https://doi.org/10.1016/j.cej.2016.08.080.
[53] O. Zakir, A. Ait Karra, R. Idouhli, M. Elyaagoubi, M. Khadiri, B. Dikici, et al., Fabrication and characterization of Ag- and Cu-doped TiO2 nanotubes (NTs) by in situ anodization method as an efficient photocatalyst, J. Solid State Electrochem. 26 (10) (2022) 2247–2260, https://doi.org/10.1007/s10008-022-05237-4.
[54] K. Nanaji, R.K. Siri Kiran Janardhana, T.N. Rao, S. Anandan, Energy level matching for efficient charge transfer in Ag doped - Ag modified TiO2 for enhanced visible light photocatalytic activity, J. Alloys Compd. 794 (2019) 662–671, https://doi.org/10.1016/j.jallcom.2019.04.283.
[55] R. Kumar, J. Rashid, M.A. Barakat, Zero valent Ag deposited TiO2 for the efficient photocatalysis of methylene blue under UV-C light irradiation, Colloids and Interface Science Communications 5 (2015) 1–4, https://doi.org/10.1016/j.colcom.2015.05.001.
[56] X.H. Yang, H.T. Fu, X.C. Wang, J.L. Yang, X.C. Jiang, A.B. Yu, Synthesis of silver-titanium dioxide nanocomposites for antimicrobial applications, J. Nanoparticle Res. 16 (8) (2014) 2526, https://doi.org/10.1007/s11051-014-2526-8.
[57] Z. Tian, L. Wang, L. Jia, Q. Li, Q. Song, S. Su, et al., A novel biomass coated Ag–TiO2 composite as a photoanode for enhanced photocurrent in dye-sensitized solar cells, RSC Adv. 3 (18) (2013) 6369–6376, https://doi.org/10.1039/C3RA40195B.
[58] B. Basumatary, R. Basumatary, A. Ramchiary, D. Konwar, Evaluation of Ag@TiO2/WO3 heterojunction photocatalyst for enhanced photocatalytic activity towards methylene blue degradation, Chemosphere 286 (2022) 131848, https://doi.org/10.1016/j.chemosphere.2021.131848.
[59] E. Albiter, M.A. Valenzuela, S. Alfaro, G. Valverde-Aguilar, F.M. Martínez-Pallares, Photocatalytic deposition of Ag nanoparticles on TiO2: metal precursor effect on the structural and photoactivity properties, J. Saudi Chem. Soc. 19 (5) (2015) 563–573, https://doi.org/10.1016/j.jscs.2015.05.009.
[60] L. Da Vià, C. Recchi, T.E. Davies, N. Greeves, J.A. Lopez-Sanchez, Visible-Light-Controlled Oxidation of Glucose using Titania-Supported Silver Photocatalysts 8 (22) (2016) 3475–3483, https://doi.org/10.1002/cctc.201600775.
[61] D. Chi, D. Sun, Z. Yang, Z. Xing, Z. Li, Q. Zhu, et al., Bifunctional nest-like self-floating microreactor for enhanced photothermal catalysis and biocatalysis, Environ. Sci.: Nano 6 (12) (2019) 3551–3559, https://doi.org/10.1039/C9EN00968J.
[62] Y. Gu, Y. Jiao, X. Zhou, A. Wu, B. Buhe, H. Fu, Strongly coupled Ag/TiO2 heterojunctions for effective and stable photothermal catalytic reduction of 4-nitrophenol, Nano Res. 11 (1) (2018) 126–141, https://doi.org/10.1007/s12274-017-1612-5.
[63] M. Thommes, K. Kaneko, A.V. Neimark, J.P. Olivier, F. Rodriguez-Reinoso, J. Rouquerol, et al., Physisorption of gases, with special reference to the evaluation of surface area and pore size distribution, IUPAC Technical Report) 87 (9–10) (2015) 1051–1069, https://doi.org/10.1515/pac-2014-1117.
[64] M. Manjunatha, H. Mahalingam, Upcycling of waste EPS beads to immobilized codoped TiO2 photocatalysts for ciprofloxacin degradation and E. coli disinfection under sunlight, Sci. Rep. 13 (1) (2023) 14631, https://doi.org/10.1038/s41598-023-41705-1.
[65] P.M. Martins, R. Miranda, J. Marques, C.J. Tavares, G. Botelho, S. Lanceros-Mendez, Comparative efficiency of TiO2 nanoparticles in suspension vs. immobilization into P(VDF–TrFE) porous membranes, RSC Adv. 6 (15) (2016) 12708–12716, https://doi.org/10.1039/C5RA25385C.
[66] M. Ren, F.H. Frimmel, G. Abbt-Braun, Multi-cycle photocatalytic degradation of bezafibrate by a cast polyvinyl alcohol/titanium dioxide (PVA/TiO2) hybrid film, J. Mol. Catal. Chem. 400 (2015) 42–48, https://doi.org/10.1016/j.molcata.2015.02.004.
[67] R. Djellabi, X. Zhao, M.F. Ordonez, E. Falletta, C.L. Bianchi, Comparison of the photoactivity of several semiconductor oxides in floating aerogel and suspension systems towards the reduction of Cr(VI) under visible light, Chemosphere 281 (2021) 130839, https://doi.org/10.1016/j.chemosphere.2021.130839.
[68] E. Falletta, M. Longhi, A. Di Michele, D.C. Boffito, C.L. Bianchi, Floatable graphitic carbon nitride/alginate beads for the photodegradation of organic pollutants under solar light irradiation, J. Clean. Prod. 371 (2022) 133641, https://doi.org/10.1016/j.jclepro.2022.133641.
[69] L. Li, Y. Li, H. Xu, W. Zhang, Novel floating TiO2 photocatalysts for polluted water decontamination based on polyurethane composite foam, Separ. Sci. Technol. 50 (2) (2015) 164–173, https://doi.org/10.1080/01496395.2014.949773.
[70] D. Cao, X. Wang, H. Zhang, D. Yang, Z. Yin, Z. Liu, et al., Rational design of monolithic g-C3N4 with floating network porous-like sponge monolithic structure for boosting photocatalytic degradation of tetracycline under simulated and natural sunlight illumination 28 (10) (2023) 3989, https://doi.org/10.3390/molecules28103989.
[71] G. Fan, J. Zhang, J. Zhan, J. Luo, J. Lin, F. Qu, et al., Recyclable self-floating A-GUN-coated foam as effective visible-light-driven photocatalyst for inactivation of Microcystis aeruginosa, J. Hazard Mater. 419 (2021) 126407, https://doi.org/10.1016/j.jhazmat.2021.126407.
[72] A.C. Swathi, S.T. Sandhiya, S. B, M. Chandran, Precursor dependent - visible light-driven g-C3N4 coated polyurethane foam for photocatalytic applications, Chemosphere 350 (2024) 141013, https://doi.org/10.1016/j.chemosphere.2023.141013.
[73] Q. Zhang, L. Jiang, J. Wang, Y. Zhu, Y. Pu, W. Dai, Photocatalytic degradation of tetracycline antibiotics using three-dimensional network structure perylene diimide supramolecular organic photocatalyst under visible-light irradiation, Appl. Catal. B Environ. 277 (2020) 119122, https://doi.org/10.1016/j.apcatb.2020.119122.
[74] W.S. Koe, J.W. Lee, W.C. Chong, Y.L. Pang, L.C. Sim, An overview of photocatalytic degradation: photocatalysts, mechanisms, and development of photocatalytic membrane, Environ. Sci. Pollut. Control Ser. 27 (3) (2020) 2522–2565, https://doi.org/10.1007/s11356-019-07193-5.
[75] F. Loosli, P. Le Coustumer, S. Stoll, Impact of alginate concentration on the stability of agglomerates made of TiO2 engineered nanoparticles: water hardness and pH effects, J. Nanoparticle Res. 17 (1) (2015) 44, https://doi.org/10.1007/s11051-015-2863-2.
[76] J. Li, J. Feng, W. Yan, Enhanced adsorption performance of PPy/TiO2 prepared on surface of TiO2 without calcination, SN Appl. Sci. 1 (6) (2019) 617, https://doi.org/10.1007/s42452-019-0628-8.
[77] S.H. Mir, B.D. Jennings, G.E. Akinoglu, A. Selkirk, R. Gatensby, P. Mokarian-Tabari, Enhanced Dye Degradation through Multi-Particle Confinement in a Porous Silicon Substrate: A Highly Efficient, Low Band Gap Photocatalyst 9 (11) (2021) 2002238, https://doi.org/10.1002/adom.202002238.
[78] D. Komaraiah, E. Radha, J. Sivakumar, M.V. Ramana Reddy, R. Sayanna, Photoluminescence and photocatalytic activity of spin coated Ag+ doped anatase TiO2 thin films, Opt. Mater. 108 (2020) 110401, https://doi.org/10.1016/j.optmat.2020.110401.
[79] D. Gogoi, A. Namdeo, A.K. Golder, N.R. Peela, Ag-doped TiO2 photocatalysts with effective charge transfer for highly efficient hydrogen production through water splitting, Int. J. Hydrogen Energy 45 (4) (2020) 2729–2744, https://doi.org/10.1016/j.ijhydene.2019.11.127.
[80] M. Humayun, F. Raziq, A. Khan, W. Luo, Modification strategies of TiO2 for potential applications in photocatalysis: a critical review, Green Chem. Lett. Rev. 11 (2) (2018) 86–102, https://doi.org/10.1080/17518253.2018.1440324.
[81] W.D. Xing, M.S. Lee, S.H. Choi, Separation of Ag(I) by ion exchange and cementation from a raffinate containing Ag(I), Ni(II) and Zn(II) and traces of Cu(II) and Sn(II) 6 (8) (2018) 112, https://doi.org/10.3390/pr6080112.
[82] T. Chen, Y. Zheng, J.-M. Lin, G. Chen, Study on the photocatalytic degradation of methyl orange in water using Ag/ZnO as catalyst by liquid chromatography electrospray ionization ion-trap mass spectrometry, J. Am. Soc. Mass Spectrom. 19 (7) (2008) 997–1003, https://doi.org/10.1016/j.jasms.2008.03.008.
[83] J. Zhu, Y. Zhu, Y. Zhou, C. Wu, Z. Chen, G. Chen, Synergistic promotion of photocatalytic degradation of methyl orange by fluorine- and silicon-doped TiO2/AC composite material 28 (13) (2023) 5170, https://doi.org/10.3390/molecules28135170.
[84] N. Nagar, V. Devra, A kinetic study on the degradation and biodegradability of silver nanoparticles catalyzed Methyl Orange and textile effluents, Heliyon 5 (3) (2019) e01356, https://doi.org/10.1016/j.heliyon.2019.e01356.
[85] R.A. Putri, S. Safni, N. Jamarun, U. Septiani, M.-K. Kim, K-d Zoh, Kinetics studies on photodegradation of methyl orange in the presence of C-N-codoped TiO2 catalyst %J Egyptian Journal of Chemistry, Innovation in Chemistry) 62 (Part 2) (2019) 563–575, https://doi.org/10.21608/ejchem.2019.14543.1883. Special Issue.
[86] C.H. Nguyen, C.-C. Fu, R.-S. Juang, Degradation of methylene blue and methyl orange by palladium-doped TiO2 photocatalysis for water reuse: efficiency and degradation pathways, J. Clean. Prod. 202 (2018) 413–427, https://doi.org/10.1016/j.jclepro.2018.08.110.
[87] S. Liang, M. An, S. Xia, B. Zhang, B. Xue, G. Xu, Enhanced photocatalytic degradation of methyl orange by TiO2/biochar composites under simulated sunlight irradiation, Opt. Mater. 142 (2023) 114105, https://doi.org/10.1016/j.optmat.2023.114105.
[88] R. Prasetyowati, E.F.M. Harahap, R.I. Saputri, P.E. Swastika, F. Fauzi, Supardi, et al., Degradation of methyl orange dye using Fe3O4/GO photocatalyst with iron derived from coastal Glagah Kulon Progo ore, Nano-Structures & Nano-Objects 38 (2024) 101153, https://doi.org/10.1016/j.nanoso.2024.101153.
[89] R. Thirugnanam, A. Kannan, S. Ramasundaram, S. Kumaravel, M. Altaf, T.H. Oh, et al., Radiant synergy: illuminating methyl orange dye removal with g-C3N4/ZnO heterojunction photocatalyst, Diam. Relat. Mater. 147 (2024) 111325, https://doi.org/10.1016/j.diamond.2024.111325.
[90] L. Predoană, E.M. Ciobanu, G. Petcu, S. Preda, J. Pandele-Cuşu, E.M. Anghel, et al., Photocatalytic performance of Sn–doped TiO2 nanopowders for photocatalytic degradation of methyl orange dye 13 (3) (2023) 534, https://doi.org/10.3390/catal13030534.